RICE UNIVERSITY

Computational Aerodynamics Modeling of the Reefed Stages of Ringsail Parachutes

by

Jason Daniel Christopher

A Thesis Submitted
in Partial Fulfillment of the
Requirements for the Degree

Master of Science

Approved, Thesis Committee:

T. E. Tezduyar, Chair
Professor of Mechanical Engineering and
Materials Science

J. E. Akin
Professor of Mechanical Engineering and
Materials Science and Professor of
Computational and Applied Mathematics

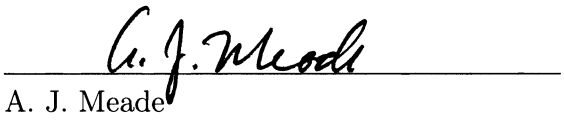

A. J. Meade
Professor of Mechanical Engineering and
Materials Science

Houston, Texas
April 2009

Report Documentation Page

Form Approved
OMB No. 0704-0188

1. REPORT DATE	2. REPORT TYPE	3. DATES COVERED
AUG 2009	**N/A**	**-**

4. TITLE AND SUBTITLE	5a. CONTRACT NUMBER
Computational Aerodynamics Modeling of the Reefed Stages of Ringsail Parachutes	5b. GRANT NUMBER
	5c. PROGRAM ELEMENT NUMBER
6. AUTHOR(S)	5d. PROJECT NUMBER
	5e. TASK NUMBER
	5f. WORK UNIT NUMBER
7. PERFORMING ORGANIZATION NAME(S) AND ADDRESS(ES) **Rice University**	8. PERFORMING ORGANIZATION REPORT NUMBER
9. SPONSORING/MONITORING AGENCY NAME(S) AND ADDRESS(ES) **The Department of the Air Force AFIT/ENEL WPAFB, OH 45433**	10. SPONSOR/MONITOR'S ACRONYM(S)
	11. SPONSOR/MONITOR'S REPORT NUMBER(S) **CI09-0047**

12. DISTRIBUTION/AVAILABILITY STATEMENT
Approved for public release, distribution unlimited

13. SUPPLEMENTARY NOTES
The original document contains color images.

14. ABSTRACT

15. SUBJECT TERMS

16. SECURITY CLASSIFICATION OF:			17. LIMITATION OF ABSTRACT	18. NUMBER OF PAGES	19a. NAME OF RESPONSIBLE PERSON
a. REPORT	b. ABSTRACT	c. THIS PAGE			
unclassified	**unclassified**	**unclassified**	**UU**	**87**	

The views expressed in this thesis are those of the author and do not reflect the official policy or position of the United States Air Force, Department of Defense, or the U. S. Government.

Abstract

Computational Aerodynamics Modeling of the Reefed Stages of Ringsail Parachutes

by

Jason D. Christopher

The Team for Advanced Flow Simulation and Modeling (T⋆AFSM) at Rice University has been using the Stabilized Space-Time Fluid-Structure Interaction (SSTFSI) they developed to model parachute aerodynamics. The complexity of ringsail parachutes requires additional techniques for successful modeling of the reefed stages. Methods developed for this purpose include sequential shape determination, which is an iterative method for determining a shape and corresponding flow field, and coupled FSI using a circumferentially symmetrized traction applied to the parachute. In addition to modeling the reefed stages, these methods provide a suitable starting point for full FSI computations. A multiscale sequentially-coupled FSI computation, together with cable symmetrization, can be used to obtain a refined structural mechanics solution where needed. Furthermore, pressure distribution generation can be used to match structural shapes to drop test observations.

Acknowledgments

I would first and foremost like to thank Dr. Tayfun Tezduyar, without whom my research experience at Rice University as a member of T⋆AFSM would not have been possible. He provided guidance throughout my stay and essential vision to my research. Dr. Tezduyar has also been a helpful source of advice professionally and personally, and I have grown a great deal during my stay at Rice due to his mentoring. I also extend my gratitude to Dr. Andrew Meade and Dr. Ed Akin for their time and efforts as members of my thesis committee.

To those whom I have worked with the past two years at T⋆AFSM, thank you for all of your patience, guidance and support. Drs. Sunil Sathe and Kenji Takizawa were both critical to my success at Rice. Your assistance elevated my research; your direction helped me progress with this research. To the many Air Force lieutenants I have had the opportunity to work with and know, I am very thankful for your service and your friendship: Lieutenants Pausewang, Schwaab, Moorman, Martin, and Wright. While at Rice, I have met people from around the world and expanded my world view because of their friendships.

To my wife, you have been there for me every day and provided invaluable support as I made progress on my research. Thank you for always understanding when I stayed late. Thank you to my dad and my sister for our weekly chats during my first move away from home. Thank you to my in-laws who were extremely helpful with everything from moving us down here to visiting and easing your daughter's time

away from Colorado.

This work was supported in part by NASA Johnson Space Center under Grant NNJ06HG84G, the Rice Computational Research Cluster funded by NSF under Grant CNS-0421109, and a partnership among Rice University, AMD and CRAY. I also acknowledge the Texas Advanced Computing Center (TACC) at The University of Texas at Austin for providing HPC resources that have contributed to the research results reported in this thesis.

Contents

List of Figures

List of Tables

Chapter 1

Introduction

Fluid–structure interaction (FSI) techniques enable researchers to investigate a variety of complex problems including blood flow through aneurysms with deformable arteries, wind-turbines with flexible blades, and parachutes made of membranes and cables. Despite this wide variety of applications, technological limitations require assumptions which render these problems tractable while still providing reasonably accurate results. In the case of parachutes, the techniques that have been developed for this purpose include the following: stand-alone structural and fluid mechanics computations are used to find a structural shape, the structure is subjected to symmetrized traction during FSI (referred to as "symmetric FSI"), porosity homogenization allows for a simpler representation of a very complex structure geometry, and where necessary multiscale sequentially-coupled FSI (SCFSI) techniques can be used in conjunction with cable symmetrization to provide a more refined structural mechanics solution. This thesis describes these techniques and provides a summary of the results obtained for offloading (reducing the payload), as a preliminary test case, and a shape determination study for the reefed stages of the parachute.

1.1 Motivation

Continuing its mission to advance human exploration, use, and development of space [8], NASA has commissioned the building of a new space system to replace the aging space shuttle and to ferry humans to even further destinations outside of Earth's orbit. This system, known as the Constellation Program, is expected to make its first operational flights early in the next decade [7]. Included in the Constellation is the Orion Crew Exploration Vehicle (CEV) which will take humans to the Moon and eventually to Mars [7]. The Constellation Program will use newly developed rockets on ascent, a method which has been popular for propelling space vehicles such as the shuttle into orbit for decades. However, the CEV will differ from the space shuttle concerning its use of parachutes to slow its return to Earth, instead of gliding as the shuttle did. The Orion CEV is based on an upscaled version of the previous Apollo system, which provides for more predictability based on historical success, popularly described by NASA as "Veteran Shape, State-of-the Art Technology" [7]. Due to the CEV's large size and fast descent, ringsail parachutes have been chosen for the Parachute Assembly System (PAS) to slow the CEV before touchdown on the earth. Ringsail parachutes are known for offering good reliability, drag efficiency and damage tolerance [5]. These very complex parachutes have many geometric features, including separate rings and sails. These components are spaced and given fullnesses in order to allow air to flow through the canopy. To maintain the fabric's integrity during the parachute's initial opening, the parachute deploys with a series of reefed stages which gradually inflate the parachute and minimize stresses experienced by the canopy. Furthermore, the reefed stages allow the system to slow down more gently which is essential for protecting the individuals on board.

To model the ringsail parachutes for the Orion system, the Team for Advanced Flow Simulation and Modeling (T$\star$AFSM) has recently employed the FSI Geometric Smoothing Technique (FSI-GST) [22] combined with porosity homogenization [25,

24]. This combination allows for a manageable computation which provides a reasonable level of accuracy. These are the primary techniques of interest when simulating offloading weight from the parachute system using FSI, as described in Section 5.2. These techniques alone, however, do not fully enable a representation of the parachute during its reefed stages nor do they account for the initial steps required prior to performing FSI. Initially, a deformed shape and developed flow field can be built using a series stand-alone structural mechanics and fluid mechanics computations, as presented in [29]. After this, a method has been developed to subject the structure to symmetrized traction from an unsteady, 3D flow field [29]. This method is used to obtain a realistic parachute shape during the reefed stages, as described in Section 5.3. Note that the more burdensome stand-alone computations normally used to build initial conditions can also provide shapes and flow fields for the shape during its reefed stages [29], and are indeed especially useful when the parachute is reefed to its smallest diameter. Furthermore, where necessary, such as when obtaining more accurate fabric stresses, a more refined structural mechanics computation can be performed using traction values from FSI computations done with a coarser structure mesh [29]. Finally, a technique is introduced to symmetrize the refined structure to aid in its deformation. These techniques stabilize the parachute and allow the modeling of more dynamic situations such as the reefed stages of the parachute.

Note that to obtain the reefed parachute configurations, a reverse sequence is used, to help convergence. In actuality, the parachute would deploy from a bag first to its Stage 1 reefing diameter, settle, then open and settle at the larger Stage 2 reefing diameter, then finally open to the fully disreefed configuration. Computationally, however, since the structural mechanics mesh is first constructed at the unstressed, quarter-sphere shape, it must be gradually changed from the fully disreefed condition to the reefed stages to make convergence easier. Trying to model the parachute's behavior using one large step between fully disreefed and the second stage reefing

diameter does not work, and thus necessitates using incremental shape determination.

Limited work has previously been performed to model parachutes during the reefed portion of their descent. The T⋆AFSM has done preliminary computations with a G–12 parachute during its reefed configuration [26], however this was a much simpler case than the ringsail parachute which is currently being investigated. The structural geometry for a G–12 is much less intricate than for a ringsail parachute, and the reefing-line ratio used is much larger, meaning the change in shape encountered in previous work was very small compared to the dramatic change observed here. These two factors make the current investigation much more complex and present numerous previously unobserved challenges.

1.2 Overview

Chapter 2 contains the governing equations used as the basis for these computations. This chapter starts with the Navier-Stokes equations of incompressible flows and ends with the equations governing the structural mechanics.

Chapter 3 provides the finite element formulations used to descretize the fluid and structural mechanics equations presented in Chapter 2. The Deforming-Spatial-Domain/Stabilized Space-Time (DSD/SST) formulation [15, 19, 20, 16] is used for solving the fluid mechanics portion of the structure/fluid system. A finite element formulation using the principle of virtual work [6, 1, 13] is used to solve the structural mechanics of the system. The Stabilized Space-Time Fluid-Structure Interaction (SSTFSI) [22] integrates both of these finite element formulations into one coupled FSI formulation.

Chapter 4 illustrates the methods used to model the parachute during its descent, especially in its reefed configurations. This chapter details the process of shape determination using stand-alone structural mechanics and fluid mechanics computations,

and describes the "symmetric FSI" technique [29] used to shield the parachute from unsymmetric forces. It also describes the improved porosity homogenization [29] used to model the geometric and fabric porosities onto an incompatible fluid interface during a disreefed and a reefed configuration. Next, it describes the Multiscale Sequentially-Coupled FSI (SCFSI) technique, which is used to obtain a more refined structural mechanics solution and hence a better distribution of the fabric stresses at Stage 2. Chapter 4 then provides a short description of the cable symmetrization technique [29], which is used in conjunction with the the multiscale SCFSI. Lastly, a technique for obtaining parachute shapes corresponding to drop test images is explained.

Chapter 5 highlights the successful implementation of the methods mentioned above. Section 5.2 presents the effects of offloading, i.e. reducing the payload, to decrease the descent speed just before landing. Section 5.3 describes in detail the results obtained for the reefed stages. Starting with an overview of the process used, it then presents results for the fully disreefed case and several intermediate reefed stages. Results for the parachute at Stage 2 computed using "symmetric FSI" are shown, along with results obtained using multiscale SCFSI. Settled Stage 1 results obtained using stand-alone structural and fluid mechanics computations are presented along with several shapes representative of the transient portion of Stage 1.

Chapter 6 provides a synopsis of the results obtained and gives conclusions relevant to the methods used to obtain those results.

Chapter 2

Governing Equations

The equations given in this chapter are at the core of the parachute simulations described in Chapter 5. This chapter begins with the Navier-Stokes equations of incompressible flow. These equations are valid for parachute simulations due to the relatively low descent velocities encountered. The chapter continues with the structural mechanics equations used to describe the parachute and cable deformations.

2.1 Fluid Mechanics

Let $\Omega_t \subset I\!R^{n_{sd}}$ be the spatial domain with boundary Γ_t at time $t \in (0, T)$. The subscript t indicates the time-dependence of the domain. The Navier–Stokes equations of incompressible flows are written on Ω_t and $\forall t \in (0, T)$ as

$$\rho \left(\frac{\partial \boldsymbol{u}}{\partial t} + \boldsymbol{u} \cdot \boldsymbol{\nabla} \boldsymbol{u} - \mathbf{f} \right) - \boldsymbol{\nabla} \cdot \boldsymbol{\sigma} = \mathbf{0} \,, \tag{2.1}$$

$$\boldsymbol{\nabla} \cdot \boldsymbol{u} = 0 \,, \tag{2.2}$$

where ρ, $\boldsymbol{u}$ and $\mathbf{f}$ are the density, velocity and the external force, respectively. The stress tensor $\boldsymbol{\sigma}$ is defined as

$$\boldsymbol{\sigma}(p, \boldsymbol{u}) = -p\mathbf{I} + 2\mu\boldsymbol{\varepsilon}(\boldsymbol{u}) \ , \tag{2.3}$$

with

$$\boldsymbol{\varepsilon}(\boldsymbol{u}) = \frac{1}{2}\left((\boldsymbol{\nabla u}) + (\boldsymbol{\nabla u})^T\right) \ . \tag{2.4}$$

Here p is the pressure, $\mathbf{I}$ is the identity tensor, $\mu = \rho\nu$ is the viscosity, ν is the kinematic viscosity, and $\boldsymbol{\varepsilon}(\boldsymbol{u})$ is the strain-rate tensor. The essential and natural boundary conditions for Eq. (2.1) are represented as

$$\boldsymbol{u} = \mathbf{g} \text{ on } (\Gamma_{\mathrm{t}})_{\mathrm{g}} \ , \tag{2.5}$$

$$\mathbf{n} \cdot \boldsymbol{\sigma} = \mathbf{h} \text{ on } (\Gamma_{\mathrm{t}})_{\mathrm{h}} \ , \tag{2.6}$$

where $(\Gamma_t)_g$ and $(\Gamma_t)_h$ are complementary subsets of the boundary Γ_t, $\mathbf{n}$ is the unit normal vector, and $\mathbf{g}$ and $\mathbf{h}$ are given functions. A divergence-free velocity field $\boldsymbol{u}_0(\mathbf{x})$ is specified as the initial condition.

2.2 Structural Mechanics

Let $\Omega_t^s \subset I\!R^{n_{xd}}$ be the spatial domain with boundary Γ_t^s, where $n_{xd} = 2$ for membranes and $n_{xd} = 1$ for cables. The superscript "s" indicates the structure. The parts of Γ_t^s corresponding to the essential and natural boundary conditions are represented by $(\Gamma_t^s)_g$ and $(\Gamma_t^s)_h$. The equations of motion are written as

$$\rho^s\left(\frac{d^2\mathbf{y}}{dt^2} + \eta\frac{d\mathbf{y}}{dt} - \mathbf{f}^s\right) - \boldsymbol{\nabla}\cdot\boldsymbol{\sigma}^s \ = \mathbf{0} \ , \tag{2.7}$$

where ρ^s, $\mathbf{y}$, $\mathbf{f}^s$ and $\boldsymbol{\sigma}^s$ are the material density, structural displacement, external force and the Cauchy stress tensor, respectively. Here η is an artificial damping coefficient, which is nonzero only in computations where time accuracy is not required, such as in determining the deformed shape of the structure for specified fluid mechanics forces acting on it. Such computations typically precede any fluid mechanics or FSI computations, and the artificial damping facilitates reaching that initial shape in a robust way. As such, structural dampening may be used during shape determination iterations, such as the final reefing configuration described later in Section 5.3.7. The stresses are expressed in terms of the second Piola–Kirchoff stress tensor $\mathbf{S}$, which is related to the Cauchy stress tensor through a kinematic transformation. Under the assumption of large displacements and rotations, small strains, and no material damping, the membranes and cables are characterized with linearly-elastic material properties. For membranes, under the assumption of plane stress, $\mathbf{S}$ becomes:

$$S^{ij} = \left(\bar{\lambda}^s G^{ij} G^{kl} + \mu^s \left(G^{il} G^{jk} + G^{ik} G^{jl}\right)\right) E_{kl} \ , \tag{2.8}$$

where for the case of isotropic plane stress $\bar{\lambda}^s = 2\lambda^s \mu^s / (\lambda^s + 2\mu^s)$. Here, E_{kl} are the components of the Green–Lagrange strain tensor, G^{ij} are the contravariant components of the metric tensor in the original configuration, and λ^s and μ^s are the Lamé constants. For cables, under the assumption of uniaxial tension, $\mathbf{S}$ becomes $S^{11} = E_c G^{11} G^{11} E_{11}$, where E_c is the Young's modulus for the cable.

Chapter 3

Finite Element Formulations

3.1 DSD/SST Formulation of Fluid Mechanics

In the Deforming-Spatial-Domain/Stabilized Space-Time (DSD/SST) method [15, 19, 20, 16, 22], the finite element formulation is written over a sequence of N space–time slabs Q_n, where Q_n is the slice of the space–time domain between the time levels t_n and t_{n+1}. At each time step, the integrations are performed over Q_n. The space–time finite element interpolation functions are continuous within a space–time slab, but discontinuous from one space–time slab to another. The notation $(\cdot)_n^-$ and $(\cdot)_n^+$ will denote the function values at t_n as approached from below and above. Each Q_n is decomposed into elements Q_n^e, where $e = 1, 2, \ldots, (n_{el})_n$. The subscript n used with n_{el} is for the general case where the number of space–time elements may change from one space–time slab to another. The essential and natural boundary conditions are enforced over $(P_n)_{\mathrm{g}}$ and $(P_n)_{\mathrm{h}}$, the complementary subsets of the lateral boundary of the space–time slab. The finite element trial function spaces $(\mathcal{S}_{\boldsymbol{u}}^h)_n$ for velocity and $(\mathcal{S}_p^h)_n$ for pressure, and the test function spaces $(\mathcal{V}_{\boldsymbol{u}}^h)_n$ and $(\mathcal{V}_p^h)_n = (\mathcal{S}_p^h)_n$ are defined by using, over Q_n, first-order polynomials in space and time. The DSD/SST formulation (as presented in [16]) is written in the following manner: given $(\boldsymbol{u}^h)_n^-$,

find $\boldsymbol{u}^h \in (\mathcal{S}_{\boldsymbol{u}}^h)_n$ and $p^h \in (\mathcal{S}_p^h)_n$ such that $\forall \mathbf{w}^h \in (\mathcal{V}_{\boldsymbol{u}}^h)_n$ and $\forall q^h \in (\mathcal{V}_p^h)_n$:

$$
\begin{aligned}
& \int_{Q_n} \mathbf{w}^h \cdot \rho \left(\frac{\partial \boldsymbol{u}^h}{\partial t} + \boldsymbol{u}^h \cdot \boldsymbol{\nabla} \boldsymbol{u}^h - \mathbf{f}^h \right) dQ + \int_{Q_n} \boldsymbol{\varepsilon}(\mathbf{w}^h) : \boldsymbol{\sigma}(p^h, \boldsymbol{u}^h) \; dQ \\
- & \int_{(P_n)_{\mathrm{h}}} \mathbf{w}^h \cdot \mathbf{h}^h \; dP + \int_{Q_n} q^h \boldsymbol{\nabla} \cdot \boldsymbol{u}^h \; dQ + \int_{\Omega_n} (\mathbf{w}^h)_n^+ \cdot \rho \left((\boldsymbol{u}^h)_n^+ - (\boldsymbol{u}^h)_n^- \right) d\Omega \\
+ & \sum_{e=1}^{(n_{el})_n} \int_{Q_n^e} \frac{1}{\rho} \left[\tau_{\mathrm{SUPG}} \rho \left(\frac{\partial \mathbf{w}^h}{\partial t} + \boldsymbol{u}^h \cdot \boldsymbol{\nabla} \mathbf{w}^h \right) + \tau_{\mathrm{PSPG}} \boldsymbol{\nabla} q^h \right] \cdot \left[\text{Ł}(p^h, \boldsymbol{u}^h) - \rho \mathbf{f}^h \right] dQ \\
+ & \sum_{e=1}^{(n_{el})_n} \int_{Q_n^e} \nu_{\mathrm{LSIC}} \boldsymbol{\nabla} \cdot \mathbf{w}^h \rho \boldsymbol{\nabla} \cdot \boldsymbol{u}^h \; dQ = 0 \; ,
\end{aligned}
\tag{3.1}
$$

where

$$
\text{Ł}(q^h, \mathbf{w}^h) = \rho \left(\frac{\partial \mathbf{w}^h}{\partial t} + \boldsymbol{u}^h \cdot \boldsymbol{\nabla} \mathbf{w}^h \right) - \boldsymbol{\nabla} \cdot \boldsymbol{\sigma}(q^h, \mathbf{w}^h) \; . \tag{3.2}
$$

This formulation is applied to all space–time slabs $Q_0, Q_1, Q_2, \ldots, Q_{N-1}$, starting with $(\boldsymbol{u}^h)_0^- = \boldsymbol{u}_0$. Here τ_{SUPG}, τ_{PSPG} and ν_{LSIC} are the SUPG (Streamline-Upwind/Petrov-Galerikin), PSPG (Pressure-Stabilizing/Petrov-Galerkin) and LSIC (least-squares on incompressibility constraint) stabilization parameters. Several different options exist to define these stabilization parameters. Here one finds the definitions given in [16]:

$$
\begin{aligned}
\tau_{\mathrm{SUPG}} &= \left(\frac{1}{\tau_{\mathrm{SUGN12}}^2} + \frac{1}{\tau_{\mathrm{SUGN3}}^2} \right)^{-\frac{1}{2}} , && (3.3) \\
\tau_{\mathrm{SUGN12}} &= \left(\sum_{a=1}^{n_{en}} \left| \frac{\partial N_a}{\partial t} + \boldsymbol{u}^h \cdot \boldsymbol{\nabla} N_a \right| \right)^{-1} , && (3.4) \\
\tau_{\mathrm{SUGN3}} &= \frac{h_{\mathrm{RGN}}^2}{4\nu} \; , && (3.5) \\
h_{\mathrm{RGN}} &= 2 \left(\sum_{a=1}^{n_{en}} |\mathbf{r} \cdot \boldsymbol{\nabla} N_a| \right)^{-1} , && (3.6) \\
\mathbf{r} &= \frac{\boldsymbol{\nabla} \| \boldsymbol{u}^h \|}{\| \; \boldsymbol{\nabla} \| \boldsymbol{u}^h \| \; \|} \; , && (3.7) \\
\tau_{\mathrm{PSPG}} &= \tau_{\mathrm{SUPG}} \; , && (3.8) \\
\nu_{\mathrm{LSIC}} &= \tau_{\mathrm{SUPG}} \; \| \boldsymbol{u}^h - \mathbf{v}^h \|^2 \; , && (3.9)
\end{aligned}
$$

where n_{en} is the number of (space–time) element nodes and N_a is the space–time shape function associated with the space–time node a. An alternative method to that shown in Eqs. (3.3)–(3.4) for determining τ_{SUPG} was presented in [22]. These options for determining τ_{SUPG} ares based on separate definitions for the advection-dominated and transient-dominated limits and are given as follows:

$$\tau_{\text{SUPG}} = \left(\frac{1}{\tau_{\text{SUGN1}}^2} + \frac{1}{\tau_{\text{SUGN2}}^2} + \frac{1}{\tau_{\text{SUGN3}}^2} \right)^{-\frac{1}{2}}, \tag{3.10}$$

$$\tau_{\text{SUGN1}} = \left(\sum_{a=1}^{n_{en}} \left| \left(\boldsymbol{u}^h - \mathbf{v}^h \right) \cdot \boldsymbol{\nabla} N_a \right| \right)^{-1}, \tag{3.11}$$

$$\tau_{\text{SUGN2}} = \frac{\Delta t}{2}, \tag{3.12}$$

where $\mathbf{v}^h$ is the mesh velocity. Note that partitioning τ_{SUGN12} into its advection-dominated and transient-dominated components as given by Eqs. (3.11)–(3.12) is equivalent to excluding the $\left(\frac{\partial N_a}{\partial t}\Big|_{\boldsymbol{\xi}} \right)$ part of $\left(\frac{\partial N_a}{\partial t} \right)$ in Eq. (3.4), making that the definition for τ_{SUGN1}, and accounting for the $\left(\frac{\partial N_a}{\partial t}\Big|_{\boldsymbol{\xi}} \right)$ part in the definition for τ_{SUGN2} given by Eq. (3.12). Here $\boldsymbol{\xi}$ is the vector of element (parent-domain) coordinates. Additional methods for calculating τ_{SUPG}, τ_{PSPG} and ν_{LSIC}, can be found in [21, 16, 17, 18]. The Discontinuity-Capturing Directional Dissipation (DCDD) stabilization, which can also be found in references [16, 17, 18], was introduced as an alternative to the LSIC stabilization.

Several of the remarks from [22] concerning this chapter are relevant and are reproduced in this thesis as Remarks 1–6.

Remark 1 *As an alternative to the way the SUPG test function is defined in Eq. (3.1), we propose the SUPG test function option of replacing the term* $\left(\frac{\partial \mathbf{w}^h}{\partial t} + \boldsymbol{u}^h \cdot \boldsymbol{\nabla} \mathbf{w}^h \right)$ *with* $\left(\left(\boldsymbol{u}^h - \mathbf{v}^h \right) \cdot \boldsymbol{\nabla} \mathbf{w}^h \right)$. *This replacement is equivalent to excluding the* $\left(\frac{\partial \mathbf{w}^h}{\partial t}\Big|_{\boldsymbol{\xi}} \right)$ *part of* $\left(\frac{\partial \mathbf{w}^h}{\partial t} \right)$. *We call this option "WTSE", and the option where the* $\left(\frac{\partial \mathbf{w}^h}{\partial t}\Big|_{\boldsymbol{\xi}} \right)$ *term is active "WTSA".*

Remark 2 *With the function spaces defined in the paragraph preceding Eq. (3.1), for each space–time slab velocity and pressure assume double unknown values at each spatial node. One value corresponds to the lower end of the slab, and the other one upper end. The option of using double unknown values at a spatial node will be called "DV" for velocity and "DP" for pressure. In this case, we use two integration points over the time interval of the space–time slab, and this time-itegration option will be called "TIP2". This version of the DSD/SST formulation, with the options set DV, DP and TIP2, will be called "DSD/SST-DP".*

Remark 3 *We propose here the option of using, for each space–time slab, a single unknown pressure value at each spatial node, and we will call this option "SP". With this, we propose another version of the DSD/SST formulation, where the options set is DV, SP and TIP2, and we will call this version "DSD/SST-SP". Because the number of unknown pressure values is halved, the computational cost is reduced substantially.*

Remark 4 *To reduce the computational cost further, we propose the option of using only one integration point over the time interval of the space–time slab, and we call this time-itegration option "TIP1". With this, we propose a third version of the DSD/SST formulation, where the options set is DV, SP and TIP1, and we will call this version "DSD/SST-TIP1".*

3.2 Semi-discrete Formulation of Structural Mechanics

Assuming that the trial function space, $\mathbf{y}^h$, and the test function space, $\mathbf{w}^h$, come from appropriately defined spaces, the semi-discrete finite element formulation of the

structural mechanics equations (see [6, 1, 13]) is written as

$$\int_{\Omega_0^s} \mathbf{w}^h \cdot \rho^s \frac{d^2\mathbf{y}^h}{dt^2}\, d\Omega^s + \int_{\Omega_0^s} \mathbf{w}^h \cdot \eta\rho^s \frac{d\mathbf{y}^h}{dt}\, d\Omega^s + \int_{\Omega_0^s} \delta\mathbf{E}^h : \mathbf{S}^h\, d\Omega^s = \int_{\Omega_t^s} \mathbf{w}^h \cdot \left(\mathbf{t}^h + \rho^s \mathbf{f}^s\right) d\Omega^s \ . \tag{3.13}$$

The fluid mechanics forces acting on the structure are represented by vector $\mathbf{t}^h$. This force term is geometrically nonlinear and thus increases the overall nonlinearity of the formulation. The left-hand-side terms of Eq. (3.13) are referred to in the original configuration and the right-hand-side terms in the deformed configuration at time t. A nonlinear system of equations emerges from this formulation at every time step. An incremental form is used to solve that nonlinear system with an iterative method (see [6, 1, 13, 3]). This form is expressed as

$$\left[\frac{\mathbf{M}}{\beta\Delta t^2} + \frac{(1-\alpha)\,\gamma\mathbf{C}}{\beta\Delta t} + (1-\alpha)\,\mathbf{K}\right] \Delta\mathbf{d}^i = \mathbf{R}^i \ . \tag{3.14}$$

Here $\mathbf{M}$ is the mass matrix, $\mathbf{C}$ is the artificial-damping matrix, $\mathbf{K}$ is the consistent tangent matrix associated with the internal elastic forces, $\mathbf{R}^i$ is the residual vector at the i^{th} iteration, and $\Delta\mathbf{d}^i$ is the i^{th} increment in the nodal displacements vector $\mathbf{d}$. The artificial-damping matrix $\mathbf{C}$, as mentioned in Section 2.2, is used only in computations where time-accuracy is not required, and for spatially-constant η it can be written as $\mathbf{C} = \eta\mathbf{M}$. All of the terms known from the previous iteration are lumped into the residual vector $\mathbf{R}^i$. The parameters α, β, γ are part of the Hilber–Hughes–Taylor [2] scheme, which is the time-integration technique used here. In the computations reported in this thesis, consistent with other parachute computations performed by the T⋆AFSM, in the structural mechanics part the mass matrix is lumped.

3.3 Stabilized Space–Time Fluid–Structure Interaction (SSTFSI) Method

The description of the SSTFSI method given here is based on the finite element formulations given by Eqs. (3.1) and (3.13), with a slight change of notation and with a clarification of how the fluid–structure interface conditions are handled. In this notation, subscripts 1 and 2 will refer to fluid and structure respectively. Furthermore, while subscript I will refer to the fluid–structure interface, subscript E will refer to "elsewhere" in the fluid and structure domains or boundaries. Then the equations representing the SSTFSI method are written as follows:

$$
\begin{aligned}
& \int_{Q_n} \mathbf{w}_{1\mathrm{E}}^h \cdot \rho \left(\frac{\partial \boldsymbol{u}^h}{\partial t} + \boldsymbol{u}^h \cdot \boldsymbol{\nabla} \boldsymbol{u}^h - \mathbf{f}^h \right) dQ + \int_{Q_n} \boldsymbol{\varepsilon}(\mathbf{w}_{1\mathrm{E}}^h) : \boldsymbol{\sigma}(p^h, \boldsymbol{u}^h) \; dQ \\
- & \int_{(P_n)_{\mathrm{h}}} \mathbf{w}_{1\mathrm{E}}^h \cdot \mathbf{h}_{1\mathrm{E}}^h \; dP + \int_{Q_n} q_{1\mathrm{E}}^h \boldsymbol{\nabla} \cdot \boldsymbol{u}^h \; dQ + \int_{\Omega_n} (\mathbf{w}_{1\mathrm{E}}^h)_n^+ \cdot \rho \left((\boldsymbol{u}^h)_n^+ - (\boldsymbol{u}^h)_n^- \right) d\Omega \\
+ & \sum_{e=1}^{(n_{el})_n} \int_{Q_n^e} \frac{1}{\rho} \left[\tau_{\mathrm{SUPG}} \rho \left(\frac{\partial \mathbf{w}_{1\mathrm{E}}^h}{\partial t} + \boldsymbol{u}^h \cdot \boldsymbol{\nabla} \mathbf{w}_{1\mathrm{E}}^h \right) + \tau_{\mathrm{PSPG}} \boldsymbol{\nabla} q_{1\mathrm{E}}^h \right] \cdot \left[\mathrm{L}(p^h, \boldsymbol{u}^h) - \rho \mathbf{f}^h \right] dQ \\
+ & \sum_{e=1}^{(n_{el})_n} \int_{Q_n^e} \nu_{\mathrm{LSIC}} \boldsymbol{\nabla} \cdot \mathbf{w}_{1\mathrm{E}}^h \rho \boldsymbol{\nabla} \cdot \boldsymbol{u}^h \; dQ = 0 \; ,
\end{aligned}
\tag{3.15}
$$

$$
\int_{Q_n} q_{1\mathrm{I}}^h \boldsymbol{\nabla} \cdot \boldsymbol{u}^h \; dQ + \sum_{e=1}^{(n_{el})_n} \int_{Q_n^e} \frac{1}{\rho} \left[\tau_{\mathrm{PSPG}} \boldsymbol{\nabla} q_{1\mathrm{I}}^h \right] \cdot \left[\mathrm{L}(p^h, \boldsymbol{u}^h) - \rho \mathbf{f}^h \right] dQ = 0 \; , \tag{3.16}
$$

$$
\int_{(\Gamma_{1\mathrm{I}})_{\mathrm{REF}}} (\mathbf{w}_{1\mathrm{I}}^h)_{n+1}^- \cdot \left((\boldsymbol{u}_{1\mathrm{I}}^h)_{n+1}^- - \boldsymbol{u}_{2\mathrm{I}}^h \right) d\Gamma = 0 \; , \tag{3.17}
$$

$$\int_{(P_n)_{\rm h}} (\mathbf{w}_{1\rm I}^h)_{n+1}^- \cdot \mathbf{h}_{1\rm I}^h \; dP = -\int_{(P_n)_{\rm h}} (\mathbf{w}_{1\rm I}^h)_{n+1}^- \cdot p\mathbf{n} \; dP + \int_{Q_n} 2\mu\boldsymbol{\varepsilon}((\mathbf{w}_{1\rm I}^h)_{n+1}^-) : \boldsymbol{\varepsilon}(\boldsymbol{u}) \; dQ + \int_{Q_n} (\mathbf{w}_{1\rm I}^h)_{n+1}^- \cdot \boldsymbol{\nabla} \cdot (2\mu\boldsymbol{\varepsilon}(\boldsymbol{u})) \; dQ, \tag{3.18}$$

$$\int_{(\Omega_{2\rm I}\,)_{\rm REF}} \mathbf{w}_{2\rm I}^h \cdot \left(\mathbf{h}_{2\rm I}^h + \left(\mathbf{h}_{1\rm I}^h\right)_{\rm A} + \left(\mathbf{h}_{1\rm I}^h\right)_{\rm B}\right) d\Omega = 0 \; , \tag{3.19}$$

$$\begin{aligned} & \int_{(\Omega_2)_0} \mathbf{w}_2^h \cdot \rho_2 \frac{d^2\mathbf{y}^h}{dt^2} \; d\Omega + \int_{(\Omega_2)_0} \mathbf{w}_2^h \cdot \eta\rho_2 \frac{d\mathbf{y}^h}{dt} \; d\Omega + \int_{(\Omega_2)_0} \delta\mathbf{E}^h : \mathbf{S}^h \; d\Omega \\ = \; & \int_{\Omega_2} \mathbf{w}_2^h \cdot \rho_2 \mathbf{f}_2^h \; d\Omega + \int_{\Omega_{2\rm E}} \mathbf{w}_{2\rm E}^h \cdot \mathbf{h}_{2\rm E}^h \; d\Omega + \int_{\Omega_{2\rm I}} \mathbf{w}_{2\rm I}^h \cdot \mathbf{h}_{2\rm I}^h \; d\Omega \; . \end{aligned} \tag{3.20}$$

Here $(\Gamma_{2\rm I}\,)_{\rm REF}$ and $(\Omega_{2\rm I}\,)_{\rm REF}$ represent some reference configurations of $\Gamma_{2\rm I}$ and $\Omega_{2\rm I}$, respectively. To bridge the slight disconnect between the slightly modified notation used here with the notation used in Eqs. (3.1) and (3.13), one should note that $\rho_2 = \rho^s$, $\mathbf{f}_2^h = \mathbf{f}^s$, $(\Omega_2)_0 = \Omega_0^s$, $\Omega_2 = \Omega_t^s$, and $\Omega_{2\rm I}$ and $\Omega_{2\rm E}$ indicate the partitions of Ω_2 corresponding to the interface and "elsewhere". It should also be noted that $\mathbf{h}_{2\rm I}^h = \mathbf{t}^h$, and $\left(\mathbf{h}_{1\rm I}^h\right)_{\rm A}$ and $\left(\mathbf{h}_{1\rm I}^h\right)_{\rm B}$ represent the values of $\mathbf{h}_{1\rm I}^h$ associated with the fluid surfaces above and below the membrane structure. The symbol $\mathbf{h}_{2\rm E}^h$ denotes the prescribed external forces acting on the structure in $\Omega_{2\rm E}$, which is separate from $\mathbf{f}_2^h$. In this formulation, $(\boldsymbol{u}_{1\rm I}^h)_{n+1}^-$, $\mathbf{h}_{1\rm I}^h$ and $\mathbf{h}_{2\rm I}^h$ (the fluid velocity, fluid stress and structural stress at the interface) are treated as separate unknowns, and Eqs. (3.17), (3.18) and (3.19) can be seen as equations corresponding to these three unknowns, respectively. The structural displacement rate at the interface, $\boldsymbol{u}_{2\rm I}^h$, is derived from $\mathbf{y}^h$.

The formulation above is based on allowing for cases when the fluid and structure

meshes at the interface are not identical. If they are identical, the same formulation can still be used. If the structure is represented by a 3D continuum model instead of a membrane model, the formulation above would still be applicable if the the domain integrations over $\Omega_{2\mathrm{E}}$ and $\Omega_{2\mathrm{I}}$ in the last two terms of Eq. (3.20) are converted to boundary integrations over $\Gamma_{2\mathrm{E}}$ and $\Gamma_{2\mathrm{I}}$. In such cases, $\mathbf{h}^h_{2\mathrm{E}}$ would represent the prescribed forces acting "elsewhere" on the surface of the structure.

Note that, for constant viscosity, the term $\boldsymbol{\nabla} \cdot (2\mu\boldsymbol{\varepsilon}(\boldsymbol{u}))$ in Eq. (3.18) vanishes for tetrahedral elements and in most cases can be neglected for hexahedral elements. The same statement can be made also in the context of that term being a part of the expression $\mathrm{Ł}(p^h, \boldsymbol{u}^h)$ appearing in Eqs. (3.15) and (3.16).

In computations which account for the porosity of the membrane fabric, Eq. (3.17) is replaced with the following one:

$$\int_{\Gamma_{1\mathrm{I}}} (\mathbf{w}^h_{1\mathrm{I}})^-_{n+1} \cdot \left((\boldsymbol{u}^h_{1\mathrm{I}})^-_{n+1} - \boldsymbol{u}^h_{2\mathrm{I}} + k_{\mathrm{PORO}} \left(\mathbf{n} \cdot \mathbf{h}^h_{1\mathrm{I}} \right) \mathbf{n} \right) d\Gamma = 0 \ , \tag{3.21}$$

where k_{PORO} is the porosity coefficient. This coefficient is typically given in units of "CFM" meaning "cubic feet of air per minute per square foot" [12]. To elaborate on this unit of measurement, when a fabric with a porosity coefficient of 1 CFM is subjected to a pressure differential of 1/2 inches of water, the amount of flow crossing is 1 ft^3/min across a sample size of 1 ft^2, which translates to a normal velocity of 1 ft/min. In the current implementation, in Eq. (3.21) only the pressure component of $\mathbf{h}^h_{1\mathrm{I}}$ is taken into account.

Remark 5 *In FSI computations with membranes and shells, the pressure at the interface has split nodal values corresponding to the fluid surfaces above and below the membrane or shell structure. We propose to use such split nodal values for pressure also at the boundaries (i.e. edges) of a membrane structure surrounded by the fluid. Our computations show that this provides additional numerical stability for the edges*

of the membrane.

Remark 6 *The versions of the SSTFSI method corresponding to the DSD/SST-DP, DSD/SST-SP, and DSD/SST-TIP1 formulations (see Remarks 2–4) will be called "SSTFSI-DP", "SSTFSI-SP", and "SSTFSI-TIP1", respectively.*

As another way of projecting the stresses from the fluid interface mesh to the structure interface mesh, whatever the transfer rule is, this thesis applies that rule to the pressure (as a scalar) and the viscous part of the stress vector separately, and combines them at the structure interface nodes by calculating the pressure part of the stress vector with unit normal vectors associated with those nodes. For future reference, this will be called "Separated Stress Projection (SSP)". To accommodate this new stress projection, a new version of the SSTFSI technique given in Section 3.3 was introduced in [24], with the pressure and viscous parts of the interface stress vectors separated. In that new version, which is denoted with the option key -SSP, the symbols $\mathbf{h}^h_{1\mathrm{I}}$ and $\mathbf{h}^h_{2\mathrm{I}}$ used in Section 3.3 would denote only the viscous parts of the stresses acting on the fluid and structure interfaces, respectively. Furthermore, in Section 3.3, the first term on the right-hand-side of Eq. (3.18) would be dropped, a scalar version of Eq. (3.19) would be added for projecting $p^h_{2\mathrm{I}}$ from $p^h_{1\mathrm{I}}$, in Eq. (3.20) $\mathbf{h}^h_{2\mathrm{I}}$ would be replaced with $-p^h_{2\mathrm{I}}\mathbf{n}+\mathbf{h}^h_{2\mathrm{I}}$, and in Eq. (3.21) $\mathbf{h}^h_{1\mathrm{I}}$ would be replaced with $-p^h_{1\mathrm{I}}\mathbf{n}+\mathbf{h}^h_{1\mathrm{I}}$.

Chapter 4

Supplementary Techniques

4.1 Shape Determination

4.1.1 Shape Determination — Overview

All fluid-structure interaction (FSI) computations require a good starting point in order to obtain reasonable results. Often, if starting conditions are not chosen carefully, the computations can progress toward unexpected results or diverge. Shape determination emerged from this realization as a way to provide both a developed and divergence-free flow field and a structural mechanics solution to start FSI computations. The method generally involves doing a stand-alone structural mechanics computation according to a prescribed pressure profile, then using this structure to create a fluid mechanics mesh. The fluid mechanics mesh is then used to do a stand-alone flow simulation from which a new pressure profile can be obtained and then applied to the structure. This iterative process continues until the structural shape changes very little when a newly computed pressure distribution is applied. At this time, FSI computations could then be started with confidence that their solution would progress in a desirable fashion.

Once its value was realized for developing a starting point for FSI computations,

the idea of shape determination next evolved as a method for modeling the shape of the ringsail parachute at the reefed configurations. The structural mechanics mesh is initially generated in the quarter-sphere shape corresponding to the unstressed state. To go directly from the unstressed shape to one where the skirt diameter is less than ten percent of the nominal diameter (as is the case for 1^{st} reefed stage) would be very difficult because of the large difference in the starting and ending shapes. Thus, a more gradual method must be used to transition the structural mechanics solution smoothly from the initial unstressed shape to the final reefed configurations. Shape determination provides an incremental approach to model these shapes.

4.1.2 Shape Determination — Details

The method involves first performing a stand-alone structural mechanics simulation according to a prescribed pressure. Then this deformed structure is used to create a fluid mesh with which to perform a stand-alone fluid mechanics computation. The flow field is solved while adjusting the descent speed until the parachute creates a steady drag which matches the system weight. The resulting flow field yields a new pressure profile which can be applied to the structure to deform it yet again. The pressure is circumferentially averaged (see Section 4.2 for more details on how it is symmetrized) to preclude rigid body motion of the parachute or an uneven inflation which might result from unbalanced forces being applied to the canopy. It is also desirable to average the pressure temporally to smoothen unsteady flow effects. Once the updated structural shape corresponding to the symmetrized pressure from the fluid computation has been found, the fluid mechanics mesh can then be deformed to match the updated shape. This deformed fluid mechanics mesh is then used in a subsequent stand-alone fluid mechanics computation. This iterative process of stand-alone structural mechanics and fluid mechanics computations continues until a final solution is achieved, whereby the parachute shape changes very little when given the

next iteration's pressure profile. The mostly unchanged shape would obviously not result in a significantly different flow field, and thus the shape and the flow field, with a converged descent speed, are considered to be finalized.

When determining the reefed parachute configuration, after the iterations yield a finalized shape for a given skirt diameter, the skirt diameter can be constricted during a stand-alone structural mechanics computation. This results in a new starting shape for another set of iterations corresponding to the new skirt diameter. At this point, a new fluid mesh can be generated if the change in diameter is large enough that it would result in unfavorable fluid element aspect ratios when deforming the original mesh.

4.2 Symmetric FSI

The initial method of shape determination described above was applied to a ringsail parachute whose parameters were provided by NASA. Parachute parameters such as the presence of a vent cap and payload weight changed over time, and thus a new shape determination study was required to obtain the reefed configuration parameters corresponding to the updated geometry. Realizing that shape determination is a very in-depth and iterative process, a more streamlined and robust approach was chosen to model this updated geometry which involves symmetrizing the traction applied to the parachute during the FSI computations; this method will be referred to as "symmetric FSI". Although the flow field corresponding to a time-dependent structure is solved every iteration in the same manner as full FSI, the traction on the fluid interface is averaged circumferentially before passing it to the structure interface. This method shields the parachute from asymmetric aerodynamic forces, which would preclude finding a steady shape while in a reefed configuration. Applying a symmetrized traction to the parachute also ensures the horizontal velocity remains negligible, which

is useful for building a starting point for full FSI in the fully disreefed configuration. In symmetrizing the horizontal effects, "symmetric FSI" eliminates any payload swing, side wind influence and gliding motion, providing a more pure representation of the nominal parachute shape in a realistic simulation true to the dynamic behavior of the parachute to include breathing.

To implement this technique, before projecting the fluid traction $\mathbf{h}_{1\mathrm{I}}^{h}$ to the structure, as shown in Section 3.3, the circumferentially-averaged fluid interface stress, $\left(\mathbf{h}_{1\mathrm{I}}^{h}\right)_{\mathrm{AVE}}$, which is symmetric with respect to the parachute axis, is calculated. Next a symmetrization ratio r_{S} is introduced and the traction is replaced by

$$(1-r_{\mathrm{S}})\mathbf{h}_{1\mathrm{I}}^{h}+r_{\mathrm{S}}\left(\mathbf{h}_{1\mathrm{I}}^{h}\right)_{\mathrm{AVE}}. \tag{4.1}$$

In the work presented here, for expedited implementation, the symmetrization of the interface stress projected to the structure and the de-symmetrization with the parameter r_{S} are done in terms of only the pressure component of the interface stress, $-p_{1\mathrm{I}}^{h}\mathbf{n}$. This expedited implementation was motivated by the "Separated Stress Projection (SSP)" introduced in [24]. Thus, the viscous forces are neglected for implementation convenience, however, these values are known to be small for high Reynolds numbers such as those encountered in parachute aerodynamics. Under fully disreefed conditions, this technique provides a periodic steady-state solution, which could then be gradually returned to full FSI computation, conditions permitting, by reducing r_{S} from 1 (corresponding to full use of the circumferential average) to 0 (corresponding to no circumferential averaging). When studying the reefed configurations, however, one can use "symmetric FSI" to obtain valid shapes and descent parameters for a given skirt diameter. It is important to note that the average parachute diameter is nearly identical for both symmetric and full FSI, and thus "symmetric FSI" does

provide an accurate representation of the parachute shape.

4.3 Homogenized Modeling of Geometric Porosity (HMGP)

4.3.1 HMGP — Overview

Parachute computations presented in this thesis have incompatible fluid and structure interface meshes. While the structure interface is true to the complex geometry used to describe the NASA ringsail parachute, the fluid interface is more simplified in order to make computations tractable. This simplification does not fundamentally alter the flow field, and thus is a reasonable approximation for obtaining aerodynamic properties concerning the parachute. The parachute's complex geometry and fabric distribution create a porosity distribution which is not easily represented by this incompatibility. The Homogenized Modeling of Geometric Porosity (HMGP) was introduced in [25, 24, 23] to accommodate this matter. The HMGP allows the intricate details and complexities of the geometric porosity to be represented using an "equivalent," locally-varying fabric porosity.

4.3.2 HMGP — Details

To obtain the homogenized geometric porosity coefficient, a four gore-model was extracted from the geometrically true structural mechanics model. This model is representative of all thirteen rings and sails of the parachute. This full geometry takes into account the slits occurring at the leading edge of rings and the fullness occurring at the leading edge of the sails. Analysis shows that due to the no-slip boundary condition at the parachute surface, insufficient flow passes through these gaps if they do not have enough elements across. Therefore, sufficient elements with

no nodes on the parachute surface must be positioned in these gaps to allow flow to be accurately modeled through these small spaces, as shown in Figure 4.1, which represents a substantial improvement over previous models. This model also accounts for flow through the parachute fabric by nodally applying manufacturer-supplied fabric porosities to the fluid interface mesh. A stand-alone fluid mechanics computation is carried out until a fully-developed flow is reached.

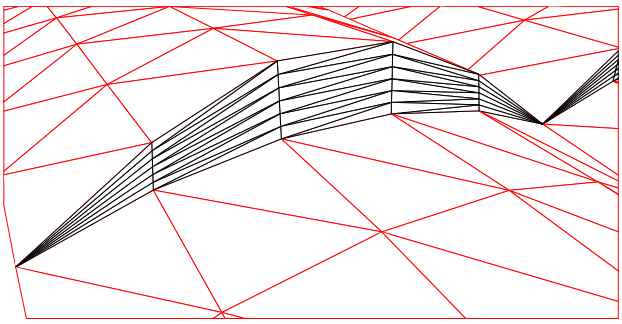

Figure 4.1: The red mesh shows the fluid interface and fluid mesh across a fullness is black.

The time-averaged flow rate through both fabric and slits/fullness is used for calculating the porosity. The canopy is divided into concentric patches and an equivalent fabric-porosity is calculated for each. Each patch includes a slit, and part of a ring or sail on either side of the slit. The porosity at the edges facing a missing sail is calculated in the same way as the porosity at the edge of the skirt is calculated, as is the case in several design cases investigated by the T⋆AFSM [14]. The porosity coefficient for the edge nodes is set to the fabric porosity, linearly progressing to the homogenized value for the adjacent patch. At the vent, the porosity coefficient for the nodes on the edge as well as those up to the node just above the middle of the first ring are set to the fabric porosity. From there, the porosity linearly progresses to the homogenized value for the adjacent patch. When a node lies on the boarder of two patches, the average porosity of two adjacent patches is applied to that node. The porosity coefficient for a patch, J, can then be calculated using the following

expression:

$$\frac{\dot{V}_J}{(A_1)_J} = -(k_{PORO})_J \frac{\Delta F_J}{(A_2)_J}. \tag{4.2}$$

Here, $\dot{V}_J$ represents the volumetric flow rate crossing patch J. It includes the flow passing through the slits as well as flow through the fabric due to material-specific porosity. The area of patch J calculated using the smoothed fluid interface is denoted by $(A_1)_J$, and the area calculated using the structure interface is denoted by $(A_2)_J$. The pressure differential seen when crossing the patch J is integrated over its area to yield a force differential denoted by ΔF_J.

4.4 Multiscale Sequentially-Coupled FSI

Fluid–Structure Interaction (FSI) computations require balancing mesh refinement and scale with the need to complete simulations whose duration is sufficient to represent at a minimum some specific period of interest (such as a heart beat for arteries or a breathing motion for a ringsail parachute). Spatially-multiscale Sequentially–Coupled FSI (SCFSI) techniques were introduced in [27, 28], whereby meshes of different refinement were used in succession. Of interest here is the version called SCFSI M1C, during which the structural shape is first computed with the coupled FSI (CFSI) technique and a relatively coarser fluid mechanics mesh, followed by mesh motion and fluid mechanics computations with a more refined mesh. By using a relatively coarser mesh at the stage where a highly-refined fluid mechanics mesh is not needed, computational effort is reserved for the final stage, where a highly-refined fluid mechanics mesh is needed to calculate the fluid mechanics quantities such as the wall shear stresses. For parachutes a derivative of this idea is used in this thesis that is spatially multiscale for the structural mechanics part. This version, as first introduced in [29], will be designated with the acronym SCFSI M2C. In this tech-

nique, one first computes the time-dependent flow field with the (fully) coupled FSI (CFSI) technique and a relatively coarser structural mechanics mesh, followed by a structural mechanics computation with a more refined mesh, with the time-dependent interface stresses coming from the previously carried out CFSI computation. With this technique, one can reduce the FSI computational effort where it is not needed and increase the accuracy of the structural mechanics computation where one needs accurate, detailed structural mechanics computations, such as computing the fabric stresses.

4.5 Cable Symmetrization

The SCFSI M2C technique presents an additional challenge of quickly bringing a parachute from its original unstressed shape to a reefed shape inflated by a traction corresponding to the specified reefing ratio. While trying to achieve a settled structural mechanics solution for these parameters, it became obvious that additional intervention was necessary. This intervention comes by way of symmetrizing the cable structure during inflation to guide the structure toward a more stable configuration. In this technique, for the cable nodes at a given latitude, components of the displacement are set in the following manner:

Tangential, θ: This component of the displacement is set to zero.

Axial, z: This component of the displacement is set to the average value for that latitude.

Radial, r: This component of the displacement is set to the average magnitude of the radial displacement.[1]

This can be done as frequently as every nonlinear iteration, or as few as just once.

[1] In the actual computations reported here, the radial component of displacement is set to the average magnitude of the total lateral displacement of all the cable nodes at a given latitude, which, when the tangential component of displacement is small, is very close to the average magnitude of the radial displacement.

Utilizing this technique during "symmetric FSI" is expected to aid computations of dynamic processes such as disreefing the parachute from one stage to the next while in an unsteady flow field.

4.6 Determination of Evolving Shapes Using Pressure Distributions

Current methods do not allow for computation of the parachute shape as it evolves in the period between its initial inflation and a time when the parachute descends settled at the Stage 1 reefed diameter. Thus, to obtain parachute shapes which match those seen at in NASA drop tests at specific instances of this dynamic period, stand-alone structural mechanics computations are performed using pressure distributions generated to approximate these shapes. Once a structural shape is computed, it is compared to NASA images and, where needed, the pressure distribution is adjusted to result in a parachute shape which more closely matches the images. This process continues until a shape is found which is sufficiently close to NASA images. T⋆AFSM's long-term objective is, using these shapes, to dynamically load the parachute to obtain information about the parachute during the opening process.

Chapter 5

Numerical Examples

The computational examples described in this chapter serve to demonstrate successful implementation of the techniques presented in Chapter 4 when used in conjunction with the core methods from Chapter 3. The parachute used for computations is an 80-gore ringsail main parachute from the NASA Orion program. Without the techniques discussed in Chapter 4, modeling this ringsail parachute would not be feasible.

5.1 80-Gore Ringsail Main Parachute

5.1.1 Main Parachute Components, Geometry and Materials

The main parachute, as described in [25, 23], has a profile of a quarter of a sphere in its unstressed shape. The crown portion of the ringsail parachute (the portion near the vent) is made of rings with gaps between the consecutive rings (see Figure 5.1). The middle and skirt portions of the parachute are made of sails. Two edges of the sails are stitched to the radial lines and the other two edges are free. The edge facing the parachute skirt is called the leading edge since this edge points toward the incoming free-stream flow as the parachute descends, and conversely, the edge facing the vent is called the trailing edge. The leading and the trailing edges could

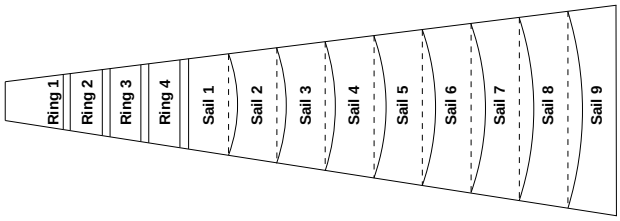

Figure 5.1: Gore layout of the ringsail parachute (not drawn to scale).

have fullnesses so that they appear to bulge out even in the unstressed geometry, as is the case with sails 1 through 8 in this particular geometry wherein the leading edges have fullness values. The ends of the leading edge of a sail coincide with the ends of the trailing edge of the next sail. The canopy construction includes several bands, lines and tapes that provide structural stiffness to the parachute. The vent band provides the necessary strength to the vent so that the parachute does not tear at the vent where the stress concentration is high. The radial lines provide stiffness along the longitudinal direction and cause the formation of the gores in the parachute. The skirt band connects the ends of the leading edges of the last sail in each gore. It can be constricted in length, which is useful for controlling the opening of the parachute. Individual sails or rings are sometimes reinforced with tapes on the leading and trailing edges to prevent tearing. The suspension lines connect the skirt end of each radial line through a confluence point to the riser, which then connects to the payload. The drag force generated in the canopy is transmitted to the payload through the suspension lines and riser. This force provides the necessary deceleration to the payload.

The ringsail parachute has 80 gores and a nominal diameter of about 120 ft. It has 4 rings and 9 sails, and together they form a quarter of a spherical surface in the unstressed configuration. The rings and sails are shown in Figure 5.1, where a single gore is laid out flat. The fullness values for the sail leading edge of each sail were provided to the T$\star$AFSM by NASA Johnson Space Center (JSC). The suspension lines are about 130 ft in length. One end of the suspension lines is connected to the

skirt-end of the radial lines and the other end is connected to the top of a single riser of about 100 ft in length. At the bottom end of the riser there is a payload weighing approximately 5,570 lbs, represented by a point mass. It has been observed that a point mass is sufficient in representing the payload; the wake effects at these low speeds combined with a relatively large distance between the payload and the parachute makes the payload's impact on the incoming air negligible [9].

The canopy of the ringsail is made of different materials. The material properties for the rings and sails were provided to the T⋆AFSM by NASA JSC. The ringsail parachute modeled here includes radial lines, suspension lines, risers, a vent band, a skirt band, and leading- and trailing-edge tapes where applicable. The material properties for these components of the ringsail were also provided by NASA JSC.

5.1.2 Geometric Smoothing

The computations presented here, as is the case in [24, 23],use incompatible meshes at the fluid–structure interface. The structure mesh is highly refined and models each individual ring, sail and gore of the parachute. Such a mesh is necessary to accurately determine the stress concentration regions, as presented in Figure 5.27. The fluid mechanics mesh at the interface is coarser. These cases use the FSI-GST described in [24] to generate and update the fluid mechanics mesh at the interface. The parachute vent is very small, and keeping one element per gore in that region would have resulted in extreme mesh refinement that would not have been affordable for flow computations. Therefore, in the circumferential direction, for the rings and sails every other valley node is picked for the fully disreefed configuration. As the parachute is reefed to its most constricted configuration, it becomes necessary to further reduce the circumferential resolution and thus every fourth valley is picked. This ensures that when the parachute is reefed, the fluid interface elements at the parachute skirt do not become too narrow. Also, one should note that for computa-

tions where a symmetrized traction is applied to the parachute (as is the case for all of the reefed cases), the fluid-interface refinement in the circumferential direction becomes less important because the traction is circumferentially averaged before being applied. To keep the element aspect ratios reasonable, in the longitudinal direction, for the first and second rings every other valley node is used. For the third ring through sixth sail every fourth valley node is used, and for each of the remaining sails every third valley node is used. Figures 5.2 and 5.3 show, for four gores, the structure and fluid meshes at the interface. Note that the fluid mesh is sufficiently refined

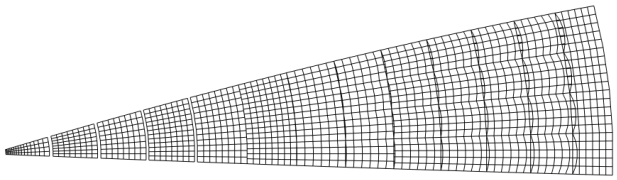

Figure 5.2: Four-gore structure mesh at the interface.

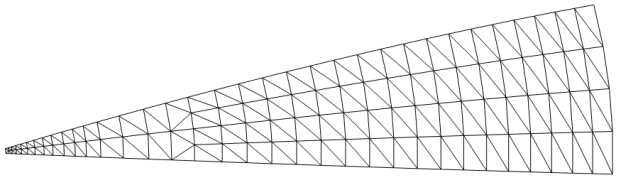

Figure 5.3: Four-gore fluid mesh at the interface.

to obtain valid flow results, but has significantly less number of nodes and elements compared to the structure mesh. Also note that the surfaces curve into the paper as one progresses toward the skirt of the parachute, and therefore the aspect ratios for the meshes near the skirt are actually even better than what they appear to be in Figures 5.2 and 5.3. The detailed views of the structure and fluid meshes for the first two rings are shown in Figures 5.4 and 5.5.

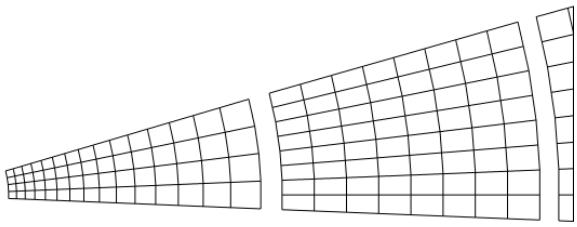

Figure 5.4: Structure mesh for the first two rings.

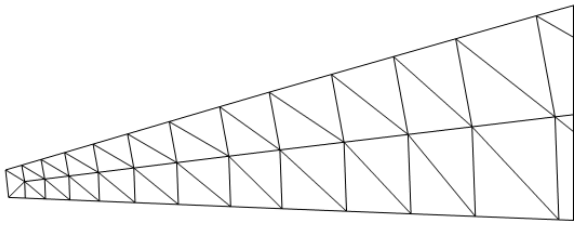

Figure 5.5: Fluid mesh for the first two rings.

5.1.3 Porosity Homogenization

All of the computations in this thesis are based on a variable porosity homogenization, as introduced in [24, 23]. In this model, the geometric porosity of the parachute structure is represented on the fluid-interface mesh with a locally-varying fabric porosity. To calculate the porosity, the canopy is divided into 12 concentric patches and an equivalent fabric-porosity coefficient is calculated for each. Each patch includes a slit, and part of a ring or sail on either side of the slit. Patch 1 includes the first ring completely, and Patch 12 includes the last sail completely. Note that the porosity coefficients match the corresponding fabric porosity at the edge of the vent and skirt. Here, fabric porosity is used because these nodes are far enough from any slits that they are modeled using only the fabric porosity. Porosity then returns linearly to the adjacent patch's homogenized porosity coefficient. Figure 5.6 shows Patch 4 of the four-gore slices of the fluid and structure interfaces. A porosity coefficient is calculated for each patch, and at the border between two patches the average of the two

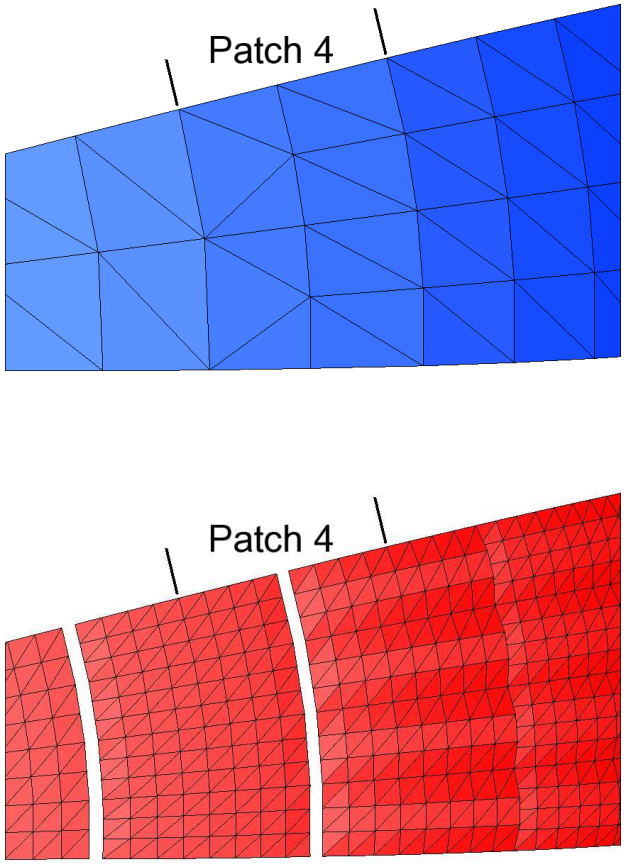

Figure 5.6: Patch 4 of the four-gore slices of the fluid (top) and structure (bottom) interfaces.

porosity coefficients is used. To calculate the porosity coefficient for each patch, a one-time flow computation at full Reynolds number is carried out, holding the canopy rigid and using a four-gore canopy slice, which fully models all the rings, sails and slits. Using only a four-gore slice, with appropriate conditions at the boundaries of the fluid volume corresponding to the slice, keeps the problem size at a manageable level when including all of the important geometric features of the canopy.

The shape of the canopy used for performing this porosity homogenization calculation comes from a series of stand-alone structural mechanics and fluid mechanics computations used to find a good starting point for fully disreefed FSI computations. For more details on the specific steps undertaken to arrive at the shape used here for

the four-gore model starting point, refer to Section 5.2.3.

The shape and descent speed resulting from the iterative process described in that section were the bases of the four-gore model presented here.

The fluid surface mesh for the four-gore slice comes from the structure mesh and has 1,562 nodes and 2,600 three-node triangular elements. The fluid volume mesh for the four-gore slice has 64,946 nodes and 360,578 four-node tetrahedral elements. The four-gore fluid surface is held rigid and the free-stream velocity is set to 25.7 ft/s, corresponding to the descent velocity used to obtain this shape. The flow computation is carried out until a fully-developed flow is reached. Figure 5.7 shows the flow field, including the flow passing through the slits.

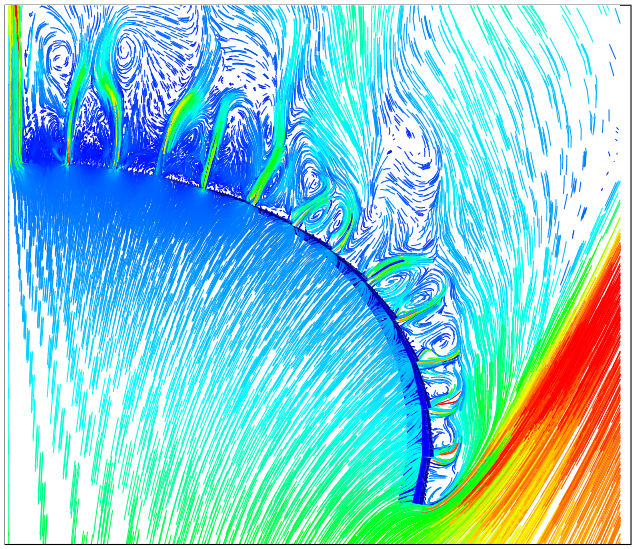

Figure 5.7: Flow field for the four-gore disreefed canopy slice with slits.

5.1.4 Porosity Homogenization: Reefed Canopy

The porosity homogenization for the fully disreefed parachute was thought to differ from that which would be obtained using a reefed parachute, so an additional flow computation was carried out with a reefed geometry configuration to determine the corresponding porosity. Under symmetrized traction conditions, which are applicable

for shape determination, the parachute's opening diameter was constricted to 43.3% of the nominal diameter, D_o, as part of the reefing procedure described in Section 5.3.4. From this geometry, another four-gore canopy slice was taken and an identical process to that in Section 5.1.3 was followed to obtain another set of porosity coefficients. For these computations, the fluid surface mesh for the four-gore slice comes from the structure mesh and has 1,582 nodes and 2,632 three-node triangular elements. The fluid volume mesh for the four-gore slice has 61,552 nodes and 339,640 four-node tetrahedral elements. The four-gore fluid surface is held rigid and the free-stream velocity is set to 37.5 ft/s, the estimated descent speed of the parachute reefed to this configuration and corresponding to the speed observed during "symmetric FSI" when reefed to 43.3%, but while still using the disreefed porosity distribution from [24, 23]. The flow computation is carried out until a fully-developed flow is reached. Figure 5.8 shows the flow field, including the flow passing through the slits. The porosity coefficient for a patch J can then be calculated by using Equation 4.2.

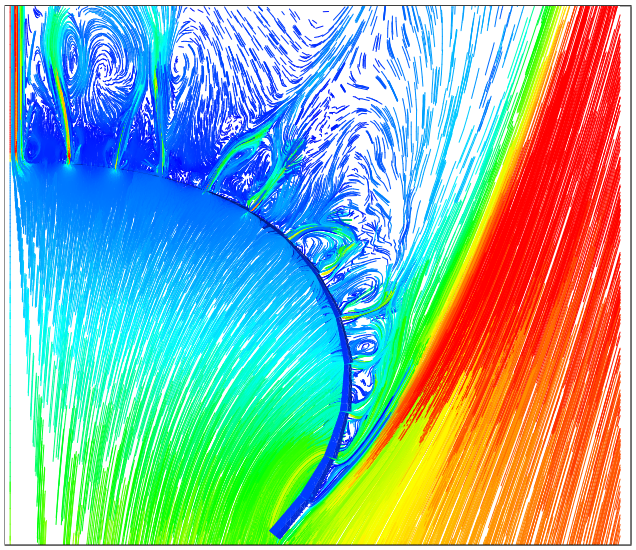

Figure 5.8: Flow field for the four-gore reefed canopy slice with slits.

After initial porosity values are calculated, the values are calibrated to ensure their net effect on parachute performance is in line with quantities known from NASA drop tests. Thus, the disreefed parachute is tested using full FSI to ensure that while gen-

erating the necessary drag it descends at a speed consistent with NASA provided drop test results. For this purpose, calibration factors of 0.9 and 0.8 were used, however, there were no striking differences between these factors so no calibration factor was applied. For the reefed configuration, no such experimental data is available, and thus an estimate for descent velocity can be made based on the decrease in skirt diameter, as dictated by the applied reefing-line ratio. For both porosity distributions shown here, the porosity values as originally calculated (i.e. calibrated by a factor of 1) allow the parachute to descend in line with expected parameters. Figures 5.9 and 5.10 show the smoothened, homogenized fluid interface colored by the porosity coefficient for the disreefed and reefed cases, respectively. Tables 5.1 and 5.2 provide the porosity coefficients for the 12 patches for the disreefed and reefed cases, respectively.

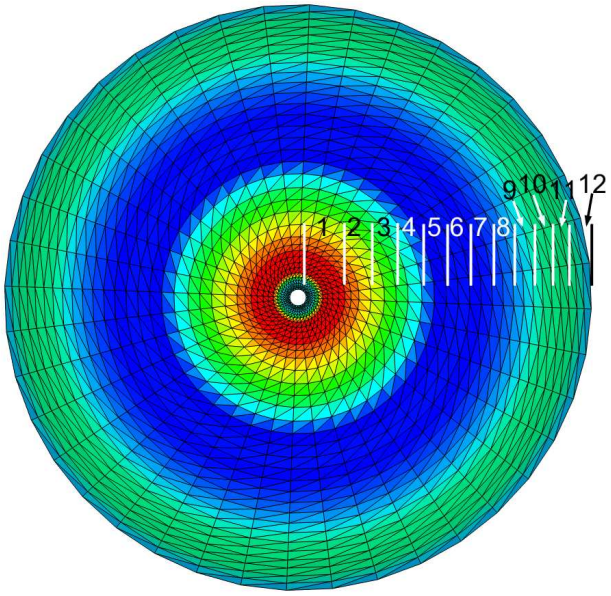

Figure 5.9: Smoothened, homogenized fluid interface colored by the porosity coefficient resulting from computations with the disreefed geometry.

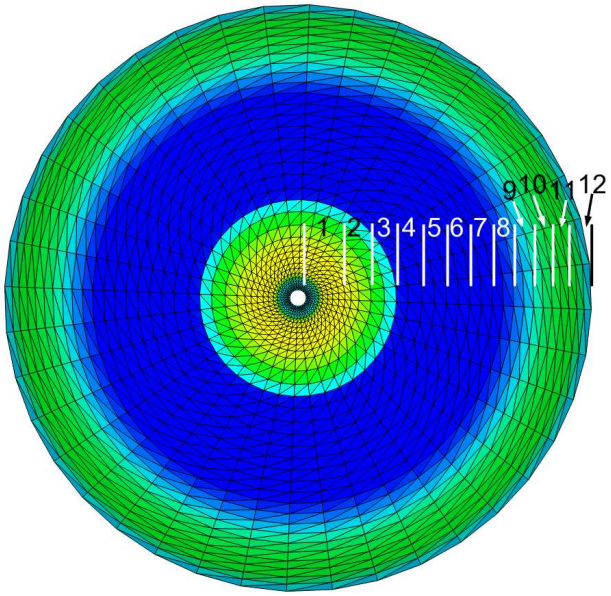

Figure 5.10: Smoothened, homogenized fluid interface colored by the porosity coefficient resulting from computations with the reefed geometry.

Patch	1	2	3	4	5	6	7	8	9	10	11	12
CFM	314	278	201	157	59	66	62	79	107	145	150	149

Table 5.1: Porosity coefficients for the 12 patches from disreefed configuration.

5.1.5 Computational Parameters

All computations reported here are carried out in a parallel computing environment, using PC clusters. All offloading computations were completed without any remeshing, whereas the reefed computations had fluid remeshing at the three most reefed configurations (i.e. when the reefing-line ratio values were 21.6%, 13% (approximately) and 7% (approximately)). All computations in this thesis were computed with moving-mesh techniques (as described in [16]) which allow the fluid mechanics mesh to move to align with the new interface boundary location. This is prefered to

Patch	1	2	3	4	5	6	7	8	9	10	11	12
CFM	248	224	165	46	49	56	52	63	100	152	171	174

Table 5.2: Porosity coefficients for the 12 patches from reefed configuration.

interface-capturing techniques which provide less accurate resolution near the fluid-structure interface [16]. One should note that the choice to remesh during reefed cases was influenced by the desire to maintain a quality mesh and high resolution near the skirt, and not by an insurmountable mesh-moving complication or tangled mesh. In fact, the results obtained after remeshing are quite similar to those obtained before remeshing, indicating the robustness of the moving–mesh techniques, even when the fluid–interface mesh at the structure boundary has large deformations. In all instances where FSI is employed, the fully-discretized, coupled fluid and structural mechanics and mesh-moving equations were solved with the quasi-direct coupling technique (see Section 5.2 in [22]). In solving the linear equation systems involved at every non-linear iteration, the Generalized Minimal RESidual (GMRES) search technique [11] was used with a diagonal preconditioner. The fluid meshes are partitioned for 64 processors to enhance the parallel efficiency of the computations. Mesh partitioning is based on the METIS [4] algorithm. Computations are carried out using SSTFSI-TIP1 technique (see Remarks 4 and 6 in Chapter 3), with the SUPG test function option WTSA (see Remark 1 in Chapter 3). The stabilization parameters used are those given by Eqs. (3.5)–(3.12), with the τ_{SUGN2} term dropped from Eq. (3.10). For boundary conditions, the outflow is set to traction free and the inflow and lateral boundaries are set to a constant freestream velocity. The parachute surface has a no-slip boundary condition. Split nodes are used for the parachute including at the vent and skirt edges, which provide for aditional numberical stability (see Remark 5 in Chapter 3). In addition to moving the reference frame vertically with a reference descent speed, the mesh is allowed to move horizontally and vertically, with the average displacement rate for the structure. This is important when the structure has significant displacement vertically compared to the reference frame, as is the case when it is reefed, or when it has large horizontal displacement as happens during full FSI once the parachute achieves a substantial lateral glide.

5.2 Offloading

5.2.1 Problem Description

The Orion space vehicle, similar to many historical spacecraft, will come down under parachutes for the last portion of its descent. Just before landing, spacecraft often use devices such as retro-rockets to slow the the vehicle, and thus, maintaining a high rate of descent while suspended beneath parachutes is not an overwhelming concern. The Orion space vehicle uses no such rockets, but rather is intended to use several large inflatable leading edge airbags to absorb some of the energy released upon impact [10]. Thus, it is anticipated that the Orion space vehicle may need to reduce its descent speed just before landing. Its estimated average descent speed of 22 ft/s may not be low enough to ensure a gentle, survivable impact. This consideration would be especially important if NASA decides to recover the space vehicle on land as opposed to on water like they did in the Apollo program. Additionally, should one of the three main parachutes fail, the CEV will descend even more rapidly. One way to reduce the descent speed at landing is to reduce the weight of the vehicle, employing a technique popularly known as "offloading". Using the FSI techniques described in [22] and more specialized techniques described in [25, 23] and this thesis, the effects of offloading are investigated. Note that the porosity coefficients used for these computations are those obtained from the fully disreefed configuration, as presented in Table 5.1. The effects of offloading are modeled using locally-varying porosity models for the homogenized and smoothened fluid interface.

5.2.2 Discretization and Mesh Properties

All computations are carried out using properties of air at standard sea-level conditions. The geometry and material properties of the structure are described in Section 5.1.1. The mesh for the structure consists of 30,722 nodes and 26,000 four-node

quadrilateral membrane elements, 12,521 two-node cable elements and one payload point mass. The membrane part of the structure forms the structure interface and has 29,200 nodes. The homogenized and smoothened fluid interface has 2,140 nodes and 4,180 elements. The fluid volume mesh for the offloading cases consists of 178,270 nodes and 1,101,643 four-node tetrahedral elements. The interface-stress projection is based on the "Separated Stress Projection (SSP)" introduced in [24]. The time-step size is 0.0232 seconds. The number of nonlinear iterations per time step is 6. The number of GMRES iterations per nonlinear iteration is 90 for the fluid and structural mechanics parts and 30 for the mesh moving part. For all six nonlinear iterations, the structure scale is set to 10 and the traction scale is set to 0.01 (for more discussion on selective scaling usage, see Remark 14 in [22]). Extra emphasis is given to the structure to help its convergence, while much less emphasis is given to traction projection equations due to their good convergence (which arises as a result of using SSP, which leaves only the viscous component of traction in this part of the computation while separating out the pressure component).

5.2.3 Offloading Procedure

The starting parachute shape and descent speed are determined by an alternating sequence of stand-alone structural mechanics and fluid mechanics computations consistent with the procedure presented in Section 4.1. Initially, the structure is inflated with a uniform pressure matching the stagnation pressure corresponding to an estimated descent speed of 25 ft/s. After this shape is achieved, a fluid mesh is constructed and a stand-alone fluid mechanics computation is performed to obtain a fully-developed flow field corresponding to this shape; the inflow velocity is set such that the drag created by the parachute matches the weight of the system. This computation uses the locally-varying fabric porosity calculated earlier in [24, 23]. Next, using the developed flow solution, a temporally and circumferentially averaged pres-

sure profile is obtained to be used for further inflating the parachute. This pressure profile is then applied to the parachute until a steady shape is reached. The iterative shape determination process, as described in Section 4.1, follows these initial steps. The process continues until a settled shape and flow field are found. Altogether, seven pairs of stand-alone structural mechanics and fluid mechanics computations were carried out. The seven pairs of computations were more than enough to have a reasonably close match between the computed drag and the total weight (payload weight plus parachute weight), at which point the descent speed was 25.7 ft/s. In addition to using them for offloading computations, the parachute shape and descent speed obtained with this sequence of stand-alone computations were also the bases for the four-gore model detailed in Section 5.1.3.

The parachute shape, descent speed and the developed flow field obtained with this sequence of stand-alone computations are used for starting "symmetric FSI", as is described in Section 4.2. Computing both the structure geometry and flow field using "symmetric FSI" continues until a settled periodic behavior is reached. In particular, the descent speed, diameter and drag are monitored until they maintain a settled, cyclic pattern of variation. The "symmetric FSI" step has a duration of 100 seconds. The first 40 seconds arere computed with the locally-varying fabric porosity calculated earlier in [24, 23], and the remaining 60 seconds are computed with the improved porosity given in Table 5.1. Once the computation reaches a settled descent with a periodic breathing motion, the pressure symmetrization is slowly removed. The de-symmetrization period is approximately 7 s, during which r_S in Equation 4.1 is varied from 1.0 to 0.0 in a Cosine form. Again, the computations are continued until a steady descent is observed. At this time, various amounts of payload are offloaded to investigate the effect on descent behavior. Using the homogenized porosity model, the ramifications of offloading 12%, 25%, 50% and 75% of the payload are considered. The largest three offloading options were chosen just for the purpose of testing the

algorithm. The smallest offloading case corresponds to the approximate weight of the heat shield, as obtained from NASA. The heat shield is approximately 12% of the weight of the vehicle and is the most likely candidate for offloading.

5.2.4 Results

As expected, the average descent speed of the payload decreases with increasing amount of offloaded weight. Specifically for the case of offloading the heat shield, the descent speed decreases by approximately 6%, in line with analytical predictions. The average drag force decreases to approximately the level of the remaining payload. Figures 5.11 and 5.12 show the descent speed and drag. Table 5.3 shows a summary of the descent characteristics for the various offloading cases. Figure 5.13 shows the flow around the parachute before the heat shield is dropped, and Figure 5.14 shows the flow around the parachute about 6 seconds after dropping the heat shield. Note that 6 seconds is approximately the duration of a single oscillation in the descent velocity of the parachute, which corresponds to the natural breathing period of the parachute structure. Figures 5.15 and 5.16 show the parachute shape before and about 6 seconds after the heat shield is dropped.

Offload Percentage	Descent Velocity (ft/s)	Drag (lbs)
0%	21.7	5670
12%	20.5	5040
25%	18.6	4340
50%	15.5	2920
75%	10.0	1550

Table 5.3: Descent characteristics for the various offloading cases.

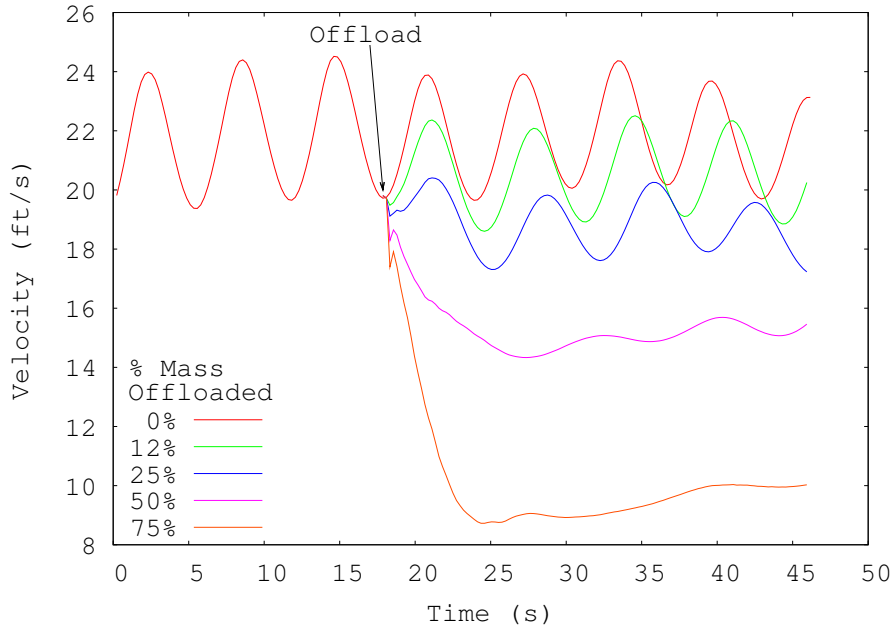

Figure 5.11: Descent speed for the offloading cases.

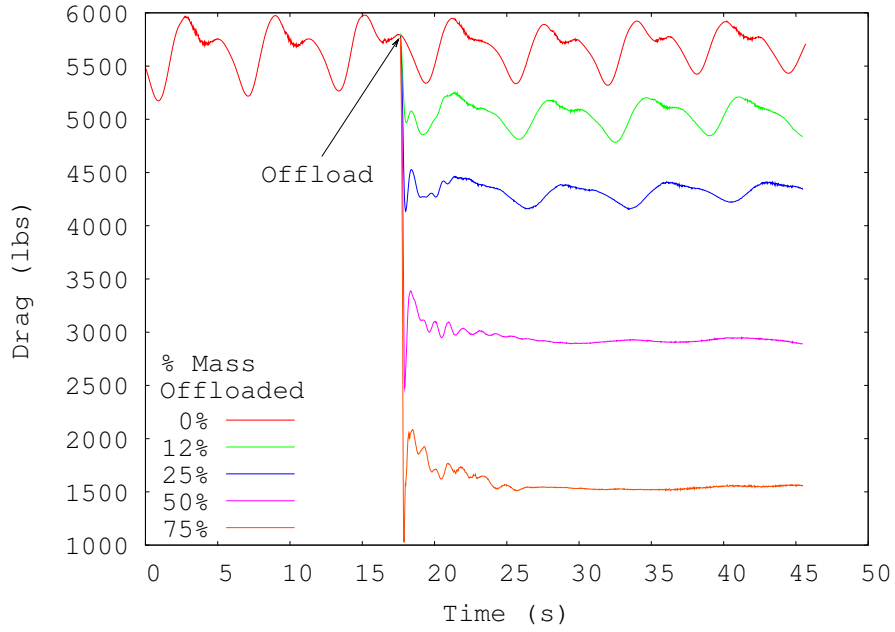

Figure 5.12: Drag for the offloading cases.

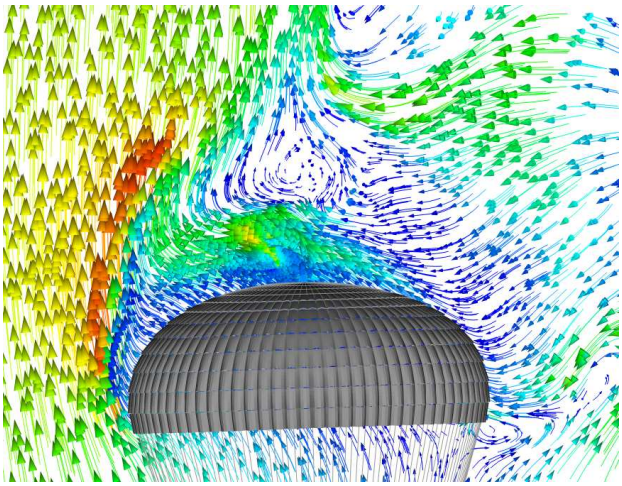

Figure 5.13: Flow past the ringsail parachute before the heat shield is dropped. The velocity vectors are colored by magnitude.

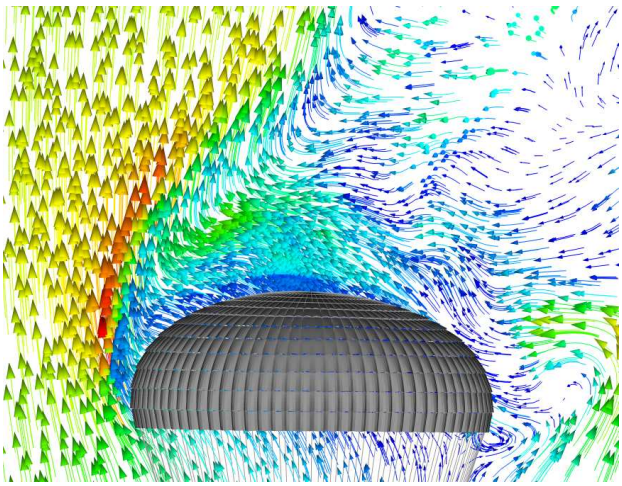

Figure 5.14: Flow past the ringsail parachute about 6 seconds after the heat shield is dropped. The velocity vectors are colored by magnitude.

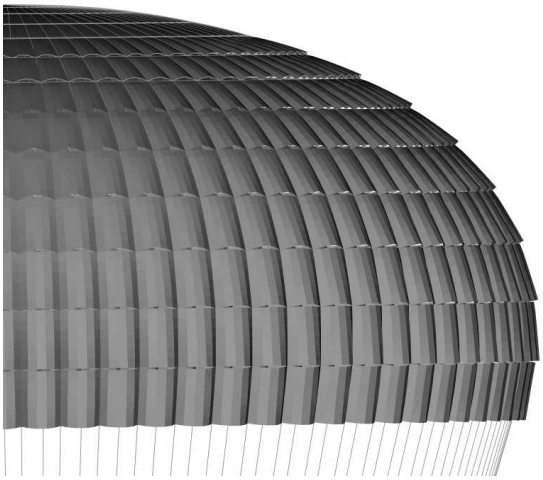

Figure 5.15: Parachute shape before the heat shield is dropped.

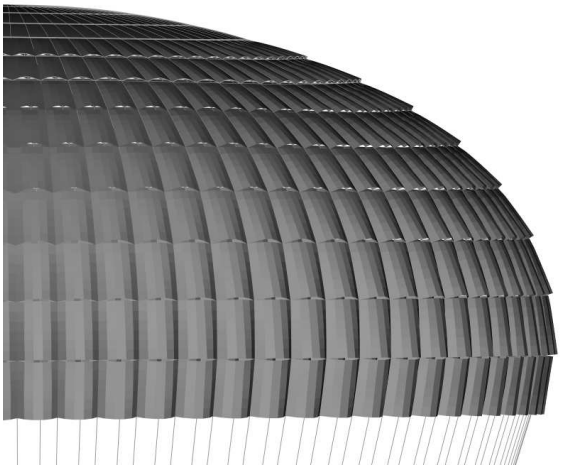

Figure 5.16: Parachute shape about 6 seconds after the heat shield is dropped.

5.3 Shape Determination for Reefed Stages

5.3.1 Problem Description

During its initial descent, the Orion space vehicle enters earth's atmosphere at a very high speed. Attempting to fully deploy the 80-gore ringsail parachutes while coming down so rapidly would likely result in parachute failures and unnecessarily high deceleration forces on the CEV structure and crew. Thus, a series of processes is undertaken to slow the vehicle enough to allow the parachutes to fully inflate and further slow the CEV to a safe speed for landing. Conical ribbon drogue parachutes first deploy to slow the vehicle down. After this, the ringsail main parachutes are deployed, but at a reefed configuration. This means that the opening diameter at the parachute's skirt is constricted to limit the amount of air flow allowed into the parachute. By limiting the initial flow, large opening shock stresses are avoided in consideration of both the parachute's integrity and the astronauts' wellbeing. Two reefed stages are used to reach a descent velocity slow enough to allow the parachute to fully inflate. During these reefed stages, the fluid dynamics and structural dynamics are very unsteady and difficult to model using current T★AFSM) techniques. The fabric tends to overlap itself easily, which can result in elements with negative volumes when trying to create or deform a fluid volume mesh. When the parachute is reefed, higher descent velocities result in larger pressure differences across the canopy near the vent and a reversal in pressure direction near the parachute skirt. These pressure gradients produce larger changes in the forces on the canopy leading to a less stable structure.

Due to these considerations, "symmetric FSI" is a necessary tool to simulate portions of the descent for the reefed stages. Furthermore, using sequential stand-alone structural mechanics and fluid mechanics computations, one can also obtain a reasonably accurate description of the parachute's shape for its reefed stages. This

technique is particularly helpful for obtaining the parachute's shape for its most reefed configuration. The entire process which leads to using these techniques is initiated with a fully disreefed parachute and followed by incrementally smaller skirt diameters until the 1st and 2nd reefed stages are achieved.

The amount by which the parachute's skirt is constrained is quantified by a value known as the "reefing-line ratio", τ_{REEF}. The reefing-line ratio is defined as:

$$\tau_{REEF} = D_{REEF}/D_o \ , \tag{5.1}$$

where D_{REEF} is the reefing-line circle diameter and D_o is the nominal parachute diameter. The reefing-line consists of a cable which attaches to the parachute skirt at every valley between adjacent gores. This is modeled using a series of cable elements to connect the skirt nodes of each valley, as shown in Figure 5.17.

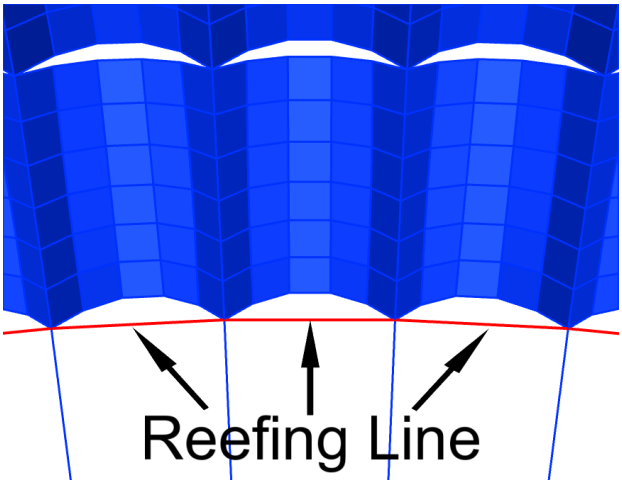

Figure 5.17: Reefing line shown in red between adjacent valleys.

NASA provided the reefing-line ratios for stages 1 and 2; their values are approximately 7% and 13%, respectively (note that a smaller reefing-line ratio indicates a smaller skirt diameter). The fully disreefed parachute configuration is not limited by a reefing line. However, based on the average diameter when the parachute is disreefed and inflated, one can calcluate a reefing-line ratio which would correspond to

this geometry; this calulation results in a τ_{REEF} value of approximately 69.0%. The intermediate τ_{REEF} values, as seen in Table 5.4, used to incrementally and gradually reef the parachute from fully disreefed to the 1st and 2nd stage τ_{REEF} values were chosen at intervals which provided for a smooth transition from one τ_{REEF} to the next.

Case	τ_{REEF}	Diameter (ft)
Fully disreefed	69.0%	80
Intermediate stage	43.3%	50
Intermediate stage	21.6%	25
Stage 2	13%	15
Stage 1	7%	8

Table 5.4: Summary of reefing-line ratios used during shape determination procedure, as well as the corresponding diameters for each τ_{REEF}. Values for Stages 1 and 2 are approximate.

5.3.2 Discretization and Mesh Properties

All computations are carried out using properties of air at standard sea-level conditions. The geometry and material properties of the structure are described in Section 5.1.1. The fluid volume mesh for the fully disreefed case consists of 99,214 nodes and 611,217 four-node tetrahedral elements. The mesh for the structure consists of 31,122 nodes and 26,320 four-node quadrilateral membrane elements, 12,441 two-node cable elements and one payload point mass. The membrane part of the structure forms the structure interface and has 29,600 nodes. Using an odd number of elements in the circumferential direction for each gore helps the mesh fold in more smoothly when it encounters a reversal in pressure difference in the reefed configuration. This structure mesh takes advantage of this consideration, which accounts for the slight difference in node and element numbers when compared to the mesh used for the offloading computations. The homogenized and smoothened fluid interface

has 1,380 nodes and 2,700 elements. Additional computational parameters are the same as those used for the offloading computations, and can be found in Section 5.2.2.

5.3.3 Fully Disreefed Parachute

As seen in the offloading computations of Section 5.2, as well as in the results reported in [24, 23, 29, 14], the ringsail parachute geometry which has been previously simulated is in the fully disreefed configuration. In all of the previous ringsail computations referenced above, there are no added modifications to constrict the skirt diameter. Therefore, the diameter's maximum value has been determined by the outward inflation of the parachute balanced by the tension in the suspension lines that pull the bottom sails toward the parachute's centerline. Preliminary discussions and investigations have been conducted using an Over Inflation Correction Line (OICL), which would influence the dynamic behavior of the parachute by constricting its maximum diameter eliminating some of the rhythmic breathing motion observed both in computational models and in NASA's drop tests. Leaving aside the investigation of OICL utilization, other cases have no fixed limitation on the diameter of the descending parachute; such is the case in this section.

The simulation sequence starts with minimal steps before subjecting the parachute to a flow field in "symmetric FSI" conditions. These steps include inflating the parachute in a stand-alone structural mechanics computation with a uniform pressure corresponding to the stagnation pressure at 26.3 ft/s, which is a reasonable pressure distribution for a fully disreefed case as shown in Figure 5.32. After this inflation, a fluid mechanics mesh is generated around the deformed structure and a stand-alone flow computation is conducted at 26.3 ft/s, which is close to a settled descent speed for the parachute based on the seven iterations described in Section 5.2.3. The porosity coefficients applied to the fluid interface come from Table 5.1. From these two stand-alone computations, a starting shape and matching developed-flow component

are achieved using a single iteration of the shape determination sequence described in Section 4.1. This is sufficient for starting "symmetric FSI" which is a robust method for reaching a settled periodic ("breathing") descent condition. Applying a circumferentially symmetrized traction to the parachute during FSI allows for a good approximation of the parachute's shape and descent characteristics. Figure 5.18 shows the shape of the parachute at a diameter which corresponds to the average of the maximum and minimum diameters experienced during this disreefed descent, while Figure 5.19 shows the flow field corresponding to this fully disreefed shape. It has been observed by the T⋆AFSM that the average diameter of the parachute is very similar in symmetric and asymmetric conditions. Thus, using a symmetrized traction provides an accurate shape compared to full FSI, and also one which is ideal without axial asymmetry. Note that this shape represents the typical shape which is observed of the Orion parachute under steady descent conditions. Despite the similarity of the shapes obtained using "symmetric FSI" and full FSI, full FSI conditions allow the parachute to obtain a horizontal glide velocity which acts to reduce the vertical velocity. This results in a coefficient of drag for full FSI which is comparable to drop test values obtained by NASA.

5.3.4 Intermediate Stage: Reefing-Line Ratio of 43.3%

The descent of the fully open parachute is computed until it reaches a settled periodic ("breathing") stage. Once the descent settles for the fully open case, which is relatively easier to compute, an incremental process of shape determination begins based on gradually shortening the reefing line to compute the parachute shape at reefed configurations. Thus, the next step is to reef the parachute to a predetermined intermediate reefing-line ratio of 43.3%. This particular τ_{REEF} value was selected because it reefs the parachute to approximately half of the constructed diameter, D_c, also known as the diameter of the unstressed or quarter-spherical geometry. One should

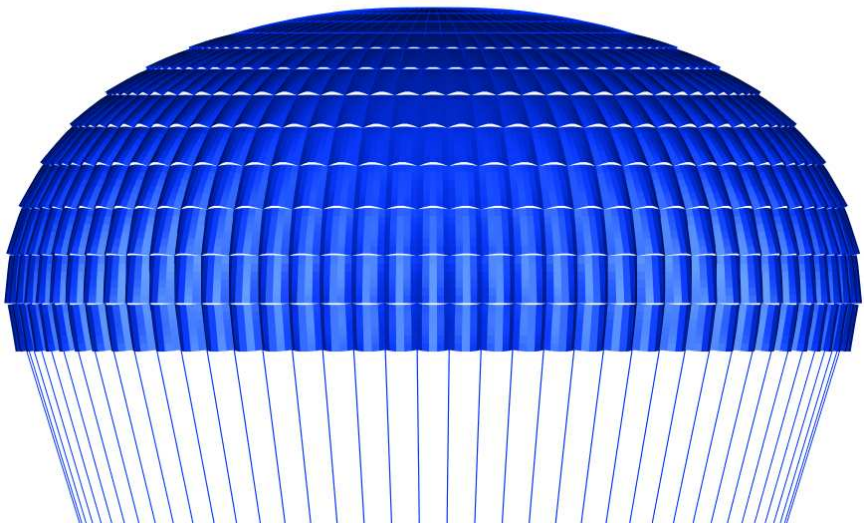

Figure 5.18: Parachute shape for a fully disreefed Orion 80-gore ringsail parachute obtained during "symmetric FSI".

note that the constructed diameter is approximately 85% of the nominal diameter, D_o.

The fully disreefed parachute's diameter fluctuations are observed until they settle down. Once settled, the parachute is gradually reefed over 400 time steps (9.28 s) from a point when the diameter was at a minimum. Gradual reefing from a point of minimum diameter serves to minimize the impact reefing the parachute has on the stable, symmetric conditions of the parachute. After constricting the parachute skirt to the new diameter, it descends in "symmetric FSI" conditions until again it achieves relatively settled drag and descent speed. One should note that the large fluctuations in descent speed and the "breathing" motion normally observed in the disreefed configuration diminish substantially when this τ_{REEF} is applied.

This τ_{REEF} value is important because it is used for calculating the homogenized porosity values used for the reefed configurations. As mentioned in Section 5.1.4, the porosity distribution for the reefed geometry differs slightly from the fully disreefed

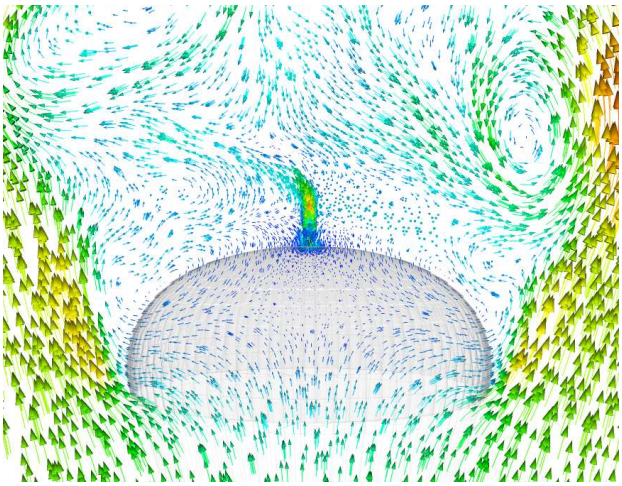

Figure 5.19: Flow field for a fully disreefed Orion 80-gore ringsail parachute. Velocity vectors colored by magnitude.

geometry. Thus, an additional calculation is carried out to quantify this difference. A τ_{REEF} value of 43.3% is used because it does not cause the parachute skirt fabric to overlap or fold in, which lead to mesh generation complications. This reefed configuration also places a portion of the fabric at the skirt of the parachute such that the free-stream flow direction nearly intersects the outside of the parachute. This distinction encompases a core difference of the disreefed and reefed configurations.

Note that for the reefing computations presented here, the porosity from Table 5.1 was used for the disreefed case and during the first reefing process. For the four-gore model, however, the shape and descent speed used in the homogenization were computed with a process that is almost the same as the process which has been described so far in this and the previous section, except that the homogenized porosity used during the course of the process is the one calculated earlier in [24, 23]. During the "symmetric FSI" computation, after reefing the parachute to a τ_{REEF} value of 43.3%, the porosity distribution is switched to the new one corresponding to the reefed configuration, as given in Table 5.2, and the computation is continued until the solution settles. All subsequent reefing computations use the porosity distribtution corresponding to the reefed configuration. The descent speed levels out at 38 ft/s

producing a coefficient of drag of 0.32, as shown in Table 5.7. Figure 5.20 shows the symmetric parachute shape, while Figure 5.21 shows the flow field corresponding to this τ_{REEF} value. The velocity vectors are colored by magnitude and scaled according to the parachute's descent velocity for this reefed stage.

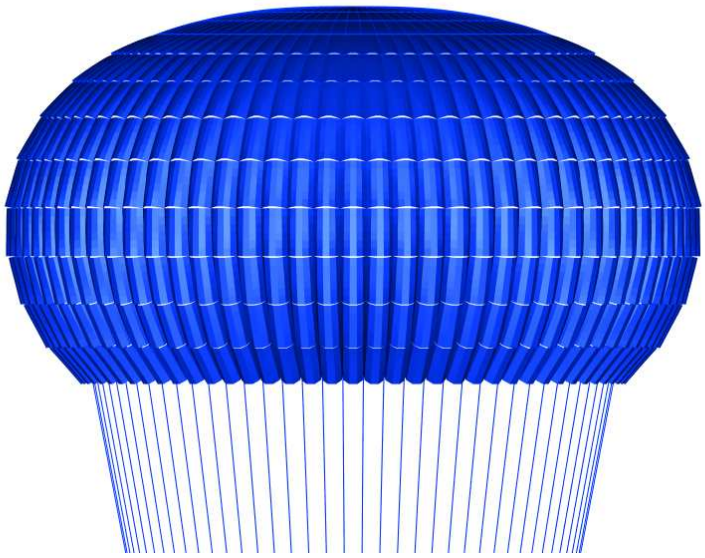

Figure 5.20: Parachute shape using a τ_{REEF} value of 43.3% and under "symmetric FSI" conditions.

5.3.5 Intermediate Stage: Reefing-Line Ratio of 21.6%

After a settled descent is reached for the parachute using a τ_{REEF} value of 43.3%, the parachute is ready to be reefed to the next configuration where the reefing-line ratio is 21.6%. This τ_{REEF} value was chosen to reef the parachute to a diameter equal to approximately half of the one preceding it; thus, the diameter at this point corresponds to approximately one quarter of D_c. The parachute is gradually reefed to a τ_{REEF} value of 21.6% over 400 time steps (9.28 s) and again given ample time for any fluctuations to settle down. Under "symmetric FSI" conditions, a steady descent speed is obtained. As was the case with parachute reefed to 43.3%, the large variations

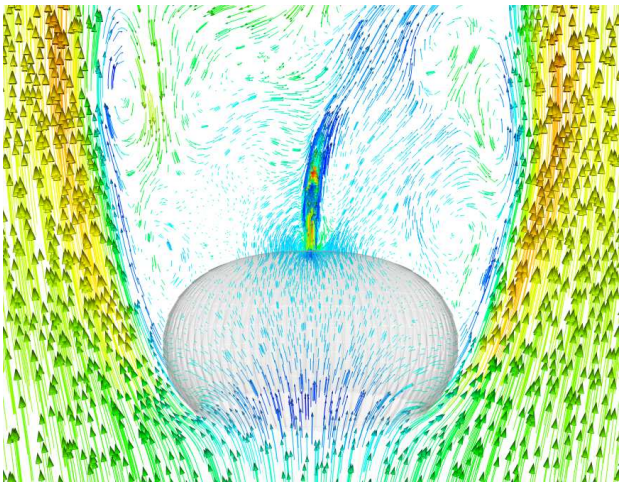

Figure 5.21: Flow field for the parachute using a τ_{REEF} value of 43.3%. Velocity vectors colored by magnitude.

in descent speed and diameter normally affiliated with the ringsail parachute does not occur in this configuration. This holds true for all of the subsequent reefed stages.

After reefing the parachute, it was observed that the fluid mechanics mesh near the skirt of the parachute was beginning to contain elements with unreasonably high aspect ratios. Thus, to ensure accurate flow results, the fluid mechanics mesh was regenerated using the same boundary elements and projecting the flow velocities and stresses to the new mesh. The new fluid volume mesh consists of 109,080 nodes and 674,099 four-node tetrahedral elements. With this τ_{REEF} value and new fluid mechanics mesh, the descent speed levels out at 52 ft/s producing a coefficient of drag of 0.17, as shown in Table 5.7. One should note that the flow field obtained using the new fluid mechanics mesh, and hence descent speed and parachute shape, differs little from the solution obtained using the original fluid mesh. Figure 5.22 shows the symmetric parachute shape, while Figure 5.23 shows the flow field for this τ_{REEF} value. The velocity vectors are colored by magnitude and scaled according to the parachute's descent velocity for this reefed stage.

Figure 5.22: Parachute shape using a τ_{REEF} value of 21.6% and under "symmetric FSI" conditions.

5.3.6 Stage 2: Reefing-Line Ratio of Approximately 13%

While the previous two reefing-line ratios were intermediate stages used to gradually reef the parachute from its fully disreefed configuration toward desired reefed diameters, the Stage 2 reefing-line ratio of approximately 13% is one of the two values which NASA actually applies during the descent of the parachute. To arrive at this shape, again a series of steps are undertaken similar to the previous reefing-line ratios. Once the descent speed settles for τ_{REEF} equal to 21.6%, the parachute is gradually reefed over 400 time steps (9.28 s) to a τ_{REEF} value equaling approximately 13%. Again it was observed that the fluid mesh elements near the outside of the parachute skirt were too stretched after reefing, resulting in unfavorably high aspect ratios. Thus, a new fluid mechanics mesh was generated having 116,879 nodes and 723,227 four-node tetrahedral elements. The fluid mechanics mesh was recreated using the same boundary elements and projecting the flow velocities and stresses to the new mesh. Using the new fluid mechanics mesh, the parachute continues to descend smoothly under

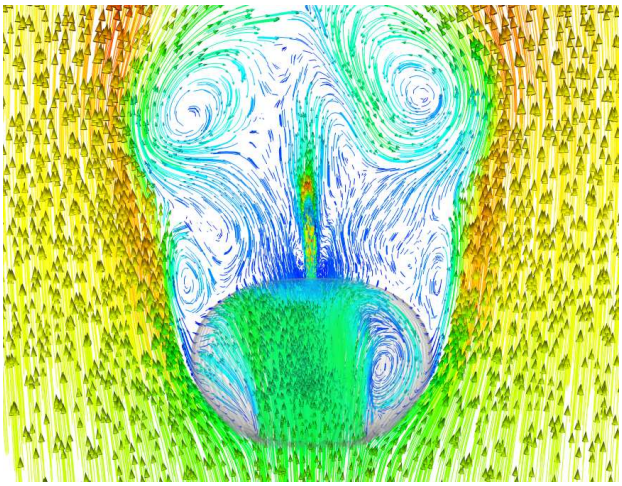

Figure 5.23: Flow field for the parachute using a τ_{REEF} value of 21.6%. Velocity vectors colored by magnitude.

"symmetric FSI" conditions. With this τ_{REEF} value of approximately 13% and new fluid mechanics mesh, the descent speed levels out at 68 ft/s producing a coefficient of drag of 0.10, as shown in Table 5.7. One should note that the flow field obtained using the new fluid mechanics mesh, and hence descent speed and parachute shape, differs little from the solution obtained using the original fluid mesh. Figure 5.24 shows the symmetric parachute shape, while Figure 5.25 shows the flow field for this τ_{REEF} value. The velocity vectors are colored by magnitude and scaled according to the parachute's descent velocity for this reefed stage.

It should be noted that all of the work up to and including this reefing-line ratio was done by applying a circumferentially symmetrized pressure during FSI. Observing the flow field shows that the pressure distribution is generally symmetric, and thus this shape determination provides a relatively good estimate for the structural shape and descent characteristics for a steady reefed condition. Allowing the pressure to be asymmetric, however, leads to the fluid mesh tangling when the structure cable elements cross. Thus, pressure symmetrization during FSI, as introduced in Section 4.2, proves itself to be a necessary tool for obtaining an accurate shape for this reefed configuration.

Figure 5.24: Parachute shape using a τ_{REEF} value of approximately 13%: Stage 2 and under "symmetric FSI" conditions..

Fabric Stress Distribution

The stress experienced by the parachute canopy fabric is of particular interest from a design perspective as this is often an important factor when deciding which material to use based on its properties. Based on a comparison of the structural displacements when reefed to the unstressed configuration, these fabric stress values can be obtained for the reefed configuration. Research done on this parachute indicates a more refined structure mesh is helpful in obtaining a more accurate stress distribution. However, comparing a refined mesh to one whose refinement is similar to the one used during the computations discussed thus far, the stress magnitudes for a given portion of the parachute are generally equivalent. Furthermore, there is little difference in shape when the same pressure profile is applied to both a coarse and a fine structure mesh. Thus, when considering this reefing level, the coarser structure mesh is sufficient for shape determination and for use during "symmetric FSI" computations, while a finer mesh is appropriate when calculating the structural fabric stress distribution. There-

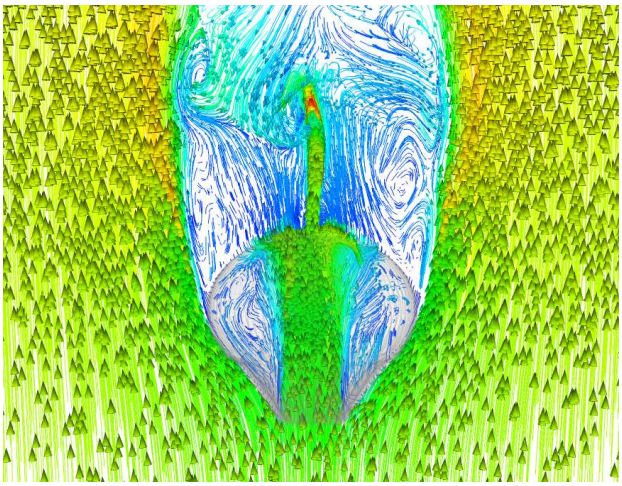

Figure 5.25: Flow field for the parachute using a τ_{REEF} value of approximately 13%: Stage 2. Velocity vectors colored by magnitude.

fore, to increase the accuracy of the structural mechanics solution for the parachute reefed to approximately 13%, the SCFSI M2C technique described in Section 4.4 is employed. Interface stresses are extracted from the "symmetric FSI" computation carried out for this reefed configuration (with the original structural mechanics mesh described above). These stresses are then used in a stand-alone structural mechanics computation with a more refined mesh. In the computations reported here, the interface stress projected to the structure consists of only the pressure component of the interface stress. The refined mesh has 128,882 nodes and 119,040 four-node quadrilateral membrane elements, 23,001 two-node cable elements and one payload point mass. The membrane part of the structure forms the structure interface and has 127,360 nodes. At this reefed configuration, the interface stresses obtained in the "symmetric FSI" computation do not have a significantly dynamic nature, and therefore time-averaged values are used.

Tables 5.5 and 5.6 outline the process used to achieve the final shape with the more refined structural mechanics mesh, and the details of the process are given here. **Step 1**: The process begins with a computation to deform the parachute from its unstressed shape to a reefed shape using a uniform pressure corresponding

to stagnation conditions at a nominal descent speed. The parachute is reefed very slowly in a linear way over the entire run to ensure a smooth transition. For all of the remaining computations, the reefing-line ratio is held constant at approximately 13%. **Step 2**: Next, a truncated version of the interface stress coming from "symetric FSI" is applied to the parachute. One should note that applying the full pressure at this point results in unfavorable and unrealistic distortion of the structure mesh, and thus this more systematic and controlled technique is employed. Truncation of the pressure profile is achieved by limiting all of the inward pressures (i.e. the pressure values near the parachute's skirt whose direction is toward the parachute's center) to a value close to zero. This computation is allowed to settle. **Step 3**: A fully symmetric shape is desirable when applying the full pressure distribution, so to help with this the "cable symmetrization" technique detailed in Section 4.5 is used. In this technique, for the cable nodes at a given latitude, the tangential component of the displacement is set to zero, and the axial component is set to the average value for that latitude. The radial component is set to the average magnitude of the radial displacement.[1] This can be done as frequently as every nonlinear iteration, or as few as just once. Here it is performed just once. **Step 4**: In addition to and following that symmetrization, the cable positions are fixed and the computation is continued until the membrane parts of the canopy structure settle. **Step 5**: After this, all the structural nodes (except for the payload) are released and the solution is computed until the structure settles. This computation requires more iterations and thus the number of time steps computed is reduced. Despite the decreased duration, the structure still achieves a very settled solution in this length of time. **Step 6**: Finally, all structural damping is removed to allow the parachute to achieve a steady solution with full and realistic parameters. The structural mechanics

[1] In the actual computations reported here, the radial component of displacement is set to the average magnitude of the total lateral displacement of all the cable nodes at a given latitude, which, when the tangential component of displacement is small, is very close to the average magnitude of the radial displacement.

solution (i.e. shape) obtained with the SCFSI M2C technique and the refined mesh is very similar to that obtained using "symmetric FSI" and the coarse mesh, as seen by comparing Figure 5.26 to Figure 5.24, however the stress distribution is slightly different(see Figure 5.27). Figure 5.28 shows a comparison of the structure obtained using the computatational methods presented here and an image of a NASA drop test of this parachute (image courtesy of NASA). This comparison clearly illustrates the similarity between computational and physical results.

Figure 5.26: Parachute shape using a fine mesh and a τ_{REEF} value of approximately 13%: Stage 2. This shape is obtained using SCFSI M2C technique.

Figure 5.27 shows the stress distribution in the parachute when reefed to a τ_{REEF} value equaling approximately 13%. The structural mechanics mesh shown on the left is the less refined mesh used during "symmetric FSI", while the mesh on the right is the more refined structure mesh. A large concentration of stress is observed near the parachute vent consistent with one's expectations, since the structurally supportive cables converge at this location. Experiments with similar parachutes confirm this trend [30]. Furthermore, the cables and tapes in the parachute provide much of the

Step #	Starting Shape	Pressure Profile	Reefing-Line Ratio
1	Unstressed	$P_{\text{stagnation}}$	Disreefed $\rightarrow$ 13%
2	Step 1	$P_{\text{“symmetricFSI”,truncated}}$	13%
3	Step 2	Symmetrize Cables	
4	Step 3	$P_{\text{“symmetricFSI”,full}}$	13%
5	Step 4	$P_{\text{“symmetricFSI”,full}}$	13%
6	Step 5	$P_{\text{“symmetricFSI”,full}}$	13%

Table 5.5: Summary of SCFSI M2C steps to go from unstressed shape to shape corresponding to traction obtained by “symmetric FSI”. This shows physical conditions used.

Step #	Time Step Size (s)	# Time Steps	Structural Damping (η)	Nonlinear Iterations	GMRES Iterations
1	0.0232	20,000	$2.155 \times 10^1 \text{s}^{-1}$	5	30
2	0.0232	20,000	$2.155 \times 10^1 \text{s}^{-1}$	5	30
3					
4	0.0232	20,000	$2.155 \times 10^2 \text{s}^{-1}$	5	30
5	0.0232	6,070	$2.155 \times 10^3 \text{s}^{-1}$	7	90
6	0.0232	4,900	0	7	90

Table 5.6: Summary of SCFSI M2C steps to go from unstressed shape to shape corresponding to traction obtained by “symmetric FSI”. This shows computational parameters used.

structural support and thus the stresses adjacent to these skeletal components are reduced.

5.3.7 Stage 1: Reefing-Line Ratio of Approximately 7%

Settled Conditions

The most reefed configuration is referred to as Stage 1. This configuration has a reefing-line ratio of approximately 7% which results in a very small opening of the skirt through which the flow may enter the canopy. As was done with the larger reefing-line ratios, to reach this final stage a starting point was chosen once the descent velocity had settled at the Stage 2 reefing-line ratio. From this point, the

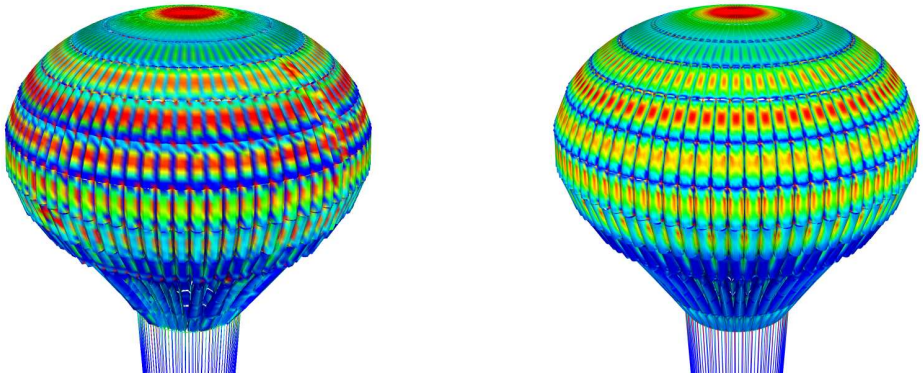

Figure 5.27: Stress distribution for the parachute using a τ_{REEF} value of approximately 13%: Stage 2. Parachute surfaces are colored by stress magnitude, with 0 and 450 lb/in^2 being the scales' minimum and maximum, respectively. Original mesh is shown on the left, while the refined mesh is shown on the right.

reefing line is gradually shortened during "symmetric FSI" to constrict the base of the parachute. The constricted geometry forces the support lines in the parachute membrane structure to be very close together making them very prone to overlap. Consequently, during this procedure the vertical lines crossed causing the fluid mesh to tangle in an unrecoverable fashion. Many parameters were investigated to preclude this occurance, however each time the parachute structure performed in a similar fashion. Thus, the original technique of shape determination using a sequence of stand-alone structural and fluid mechanics computations, as presented in Section 4.1, was finally employed.

The structure was reefed in a stand-alone structural mechanics computation from the converged Stage 2 geometry to a geometry using the reefing-line ratio for Stage 1. The pressure distribution applied to the structure came from an initial implementation of the shape determination concept for reefing, which used the same 80-gore ringsail parachute but with the addition of a vent cap. This is thought to be a good starting pressure distribution since it corresponds to a finalized distribution for the slightly different previous geometry. Structural damping is used to help achieve this steady shape, consistent with its appropriate application described in Section 2.2;

Figure 5.28: Comparison of results obtained using computational tools (specifically resulting from "symmetric FSI" and M2C SCFSI) to NASA provided drop test.

the damping coefficient η is set to 21 s^{-1}. Once a shape is achieved with this initial pressure and reefing-line ratio, the first structure iteration is complete. To further prevent the fluid mechanics mesh from tangling in future computations, a coarser fluid interface mesh is used. This mesh decreases the circumferential refinement at the skirt of the parachute consistent with the description detailed in Section 5.1.2, resulting in a mesh with 1,180 nodes and 2,320 triangular elements. Based on the shape coming from the first structure iteration a fluid mesh is constructed. It contains 117,613 nodes and 728,965 four-node tetrahedral elements. Stand-alone fluid mechanics computations are performed to obtain a developed flow solution for the geometry. The inflow velocity is adjusted until the parachute drag matches the weight of the system. A short "symmetric FSI" computation was attempted using this shape and flow field, but it progressed only a short period (less than one physical second) before tangling. The resulting flow field and structural shape from this computation are used as the starting points for the subsequent stand-alone structural mechanics and fluid mechanics computations. The flow field is used to create a temporally and circumferentially averaged pressure profile to apply to the parachute in a stand-alone

structural mechanics computation to achieve a new shape. The fluid mesh is deformed to match the new structure location (no remeshing was performed during this shape determination process) and a subsequent fluid-only computation is performed. As described in detail in Section 4.1, this process continues until a constant shape and velocity are found. Altogether, four pairs of stand-alone structural mechanics and fluid mechanics computations were carried out.

With this τ_{REEF} value of approximately 7%, the descent speed was found to be 103 ft/s producing a coefficient of drag of 0.04, as shown in Table 5.7. The final shape is shown in Figure 5.29, along with the initial shape corresponding to the original pressure profile as obtained from previous computations with a slightly different geometry and a shape from an intermediate step. Figure 5.30 shows the flow field for this τ_{REEF} value, corresponding to the Stage 1 reefing configuration and the shape on the right side of Figure 5.29. The velocity vectors are colored by the magnitude and scaled according to the parachute's descent velocity for this reefed stage. This parachute shape and the resulting flow characteristics represent the parachute descending for an extended duration at the prescribed reefing-line ratio, hence the title of this subsection: Settled Conditions. Of additional interest to NASA are the characteristics of the parachute between when it is first inflated and when it reaches steady descent conditions for Stage 1. This period during the parachute's initial inflation is addressed next.

Determination of Evolved Shapes

To model the parachute's behavior for its first stage reefing-line ratio before it reaches a settled descent, NASA images were studied to first gain a better understanding of the shapes observed during this time. Based on these shapes, pressure profiles were generated which, when applied to the structural mechanics mesh, result in mesh deformation which causes the structural shape to be similar to the observations. The

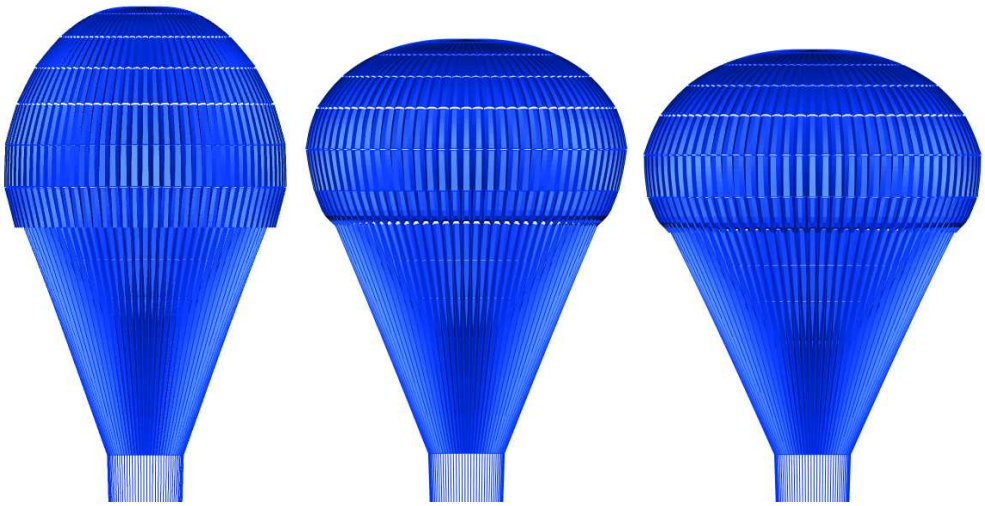

Figure 5.29: Parachute shapes using a τ_{REEF} value of approximately 7%: Stage 1. Left: structural shape based on original pressure distribution from slightly different geometry. Middle and right: structural shapes from series of stand-alone structural and fluid mechanics computations; middle image is an intermediate step, and right image is finalized shape.

pressure distribution which results in the final shape is found iteratively, as described in Section 4.6. Several of the shapes found based on NASA images are shown in Figure 5.31. The T⋆AFSM)'s long-term objective is to find a way to dynamically change from one shape to another over a duration representative of the physical process. This would provide a better understanding of the dynamic stresses experienced by the canopy during disreefing.

5.3.8 Summary for the Reefed Stages

Modeling the reefed stages of NASA's Orion 80-gore ringsail parachute requires special techniques including shape determination and "symmetric FSI". Table 5.7 provides a summary of the descent characteristics obtained through modeling the reefed parachute. The trends shown in Table 5.7 match expectations. Furthermore, Figure 5.32 shows the pressure profiles obtained through this analysis. Theses curves

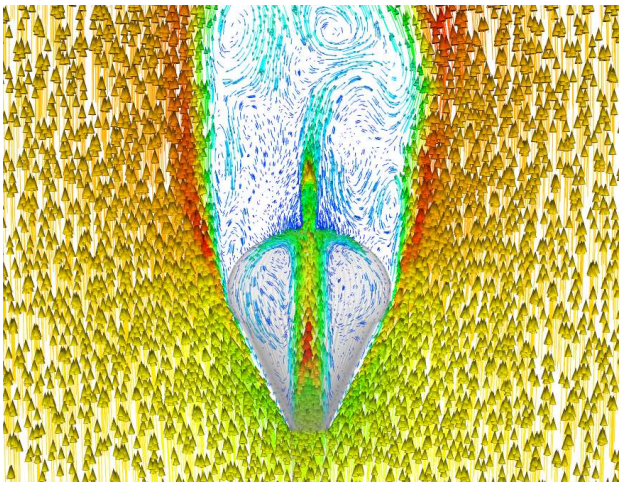

Figure 5.30: Flow field for the parachute using a τ_{REEF} value of approximately 7%: Stage 1. Velocity vectors colored by magnitude.

represent the temporally and circumferentially averaged pressure difference across the canopy versus the distance from the canopy's vent. Note that a positive pressure difference indicates the pressure inside is larger than the pressure outside of the parachute. The pressure profile for the fully disreefed case is essentially flat indicating that the pressure distribution is nearly uniform from the vent to the skirt. As the parachute is reefed, however, the pressure difference toward the skirt gradually begins to fall as the outside of the parachute starts to face into the incoming free stream air. This pressure difference eventually becomes negative, at which point the parachute experiences a reversal in its normal bulge direction; the sails bulge toward the parachute's center when the pressure difference is negative, i.e. the pressure is higher on the outside. As the diameter continues to decrease, the drag area of the parachute also decreases. For steady descent where drag matches weight in these reefed conditions, the pressure difference which acts on the surface in a direction opposing gravity must increase. This explains the increase in pressure differential toward the vent of the parachute, where the majority of the drag is created, especially in cases with smaller reefing-line ratios.

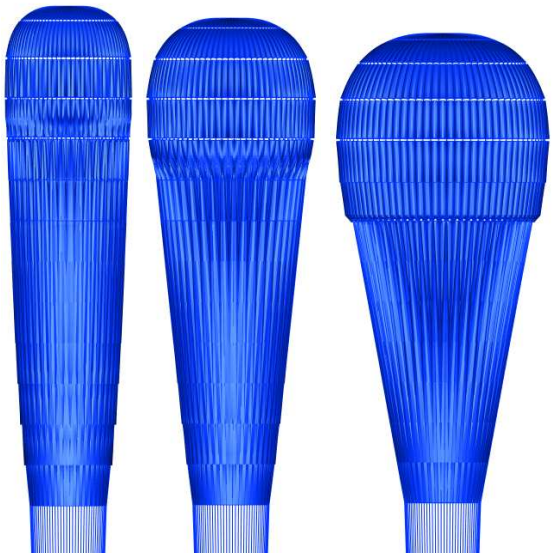

Figure 5.31: Parachute shapes using a τ_{REEF} value of approximately 7%: Stage 1. Results from stand-alone structural mechanics computations where pressure profiles are generated to match shapes observed during NASA drop tests. From left to right, shapes show progression of shape during this reefed stage.

Reefing-line Ratio	Descent Velocity (ft/s)	Coefficient of Drag
69.0%	24	0.77
43.3%	38	0.32
21.6%	52	0.17
13%	68	0.10
7%	103	0.04

Table 5.7: Descent characteristics for the investigated reefing ratios. Reefing-line ratios for Stages 1 and 2 are approximate.

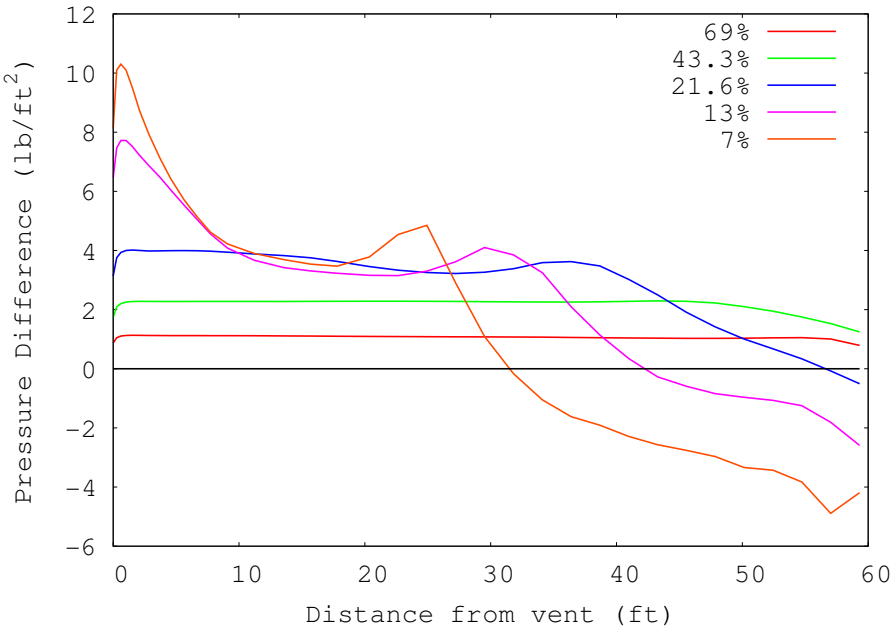

Figure 5.32: Pressure distributions versus distance from the parachute vent for the studied reefing-line ratios. Note that 13% and 7% are approximate values.

Chapter 6

Conclusions

The computations presented in this thesis show that analyzing a parachute's descent can be accomplished using the sophisticated FSI methods developed by the T⋆AFSM combined with new special purpose techniques. Shape determination by way of stand-alone structural mechanics and fluid mechanics computations allows for a successful understanding of the static shape of a ringsail parachute when reefed to various levels. Shape determination is also helpful as a tool to determine a valid starting point for FSI computations. "Symmetric FSI" offers a more robust and less burdensome method for building a good starting point for full FSI computations or for characterizing the parachute's shape in a way that eliminates any unsymmetric parachute deformation or gliding. Homogenized Modeling of Geometric Porosity (HMGP) proves a useful tool for completing computations using a less refined fluid interface mesh while still retaining a structure mesh true to the parachute geometry. Furthermore, as the parachute changes shapes it is important to characterize the influence this has on parachute porosity, as is done in this thesis. Lastly, with the intention of decreasing computational cost where it is not needed, the Multiscale Sequentially-Coupled FSI (SCFSI) technique allows for the use of a coarser structural mechanics mesh during FSI, followed by the use of a more refined structural

mechanics mesh to compute quantities sensitive to mesh refinement, such as stress distribution. Cable symmetrization proves to be a necessary tool for deforming the more refined mesh during SCFSI M2C.

Two test cases were presented to show the necessity of using the techniques described above in order to analyze complex stages and events during a ringsail parachute's descent. The first test case investigates the effect of offloading various amounts of payload weight. Shape determination was used to build a starting shape, developed flow field and descent velocity for these offloading computations, as well as a porosity calculation which improved the representation of geometric and fabric porosity on the smoothened fluid interface. "Symmetric FSI" was used to further build a starting point for full FSI. During full FSI, the solution was allowed to settle and the various amounts were offloaded resulting in a decrease in drag equivalent to the amount of payload offloaded. Descent velocity also decreased according to the amount of payload offloaded. This work demonstrates the ability of these methods to model design implementations and changes to the parachute which might improve the system's performance. Based on these computations, NASA has a better understanding of its options during Orion's actual descent.

The next test case involves characterizing the ringsail parachute during its initial phases of descent, while it is reefed to its 1^{st} and 2^{nd} Stages. This work helps to characterize descent parameters such as vertical velocity and coefficient of drag, as well as the shape during the reefed stages of the parachute. Both shape determination and "symmetric FSI" are effective tools for simulating the parachute when reefed, while HMGP is able to accommodate changes in the parachute's shape to accurately model the porosity distribution while reefed. Understanding the parachute's descent during these stages is very important for determining fabric loads and SCFSI M2C, when combined with cable symmetrization, enables computation of a refined stress distribution. Furthermore, a better understanding of the parachute's shapes during

the dynamic inflation and disreefing processes, along with the corresponding pressure distributions, can be obtained by generating pressures, which when applied to the structure, result in structural shapes which closely match NASA images. Based on these methods, one can successfully analyze a ringsail parachute even during the complex stages of descent.

Bibliography

[1] R. Benney, K. Stein, J. Leonard, and M. Accorsi. Current 3-D structural dynamic finite element modeling capabilities. In *Proceedings of AIAA 14th Aerodynamic Decelerator Systems Technology Conference*, AIAA Paper 97-1506, San Francisco, California, 1997.

[2] H. Hilber, T. Hughes, and R. Taylor. Improved numerical dissipation for time integration algorithms in structural dynamics. *Earthquake Engineering and Structural Dynamics*, 5:283–292, 1977.

[3] V. Kalro and T. Tezduyar. A parallel 3D computational method for fluid–structure interactions in parachute systems. *Computer Methods in Applied Mechanics and Engineering*, 190:321–332, 2000.

[4] G. Karypis and V. Kumar. A fast and high quality multilevel scheme for partitioning irregular graphs. *SIAM Journal of Scientific Computing*, 20:359–392, 1998.

[5] T. W. Knacke. *Parachute Recovery Systems: Design Manual*. Para Publishing, Santa Barbara, CA, 1992.

[6] A. Lo. *Nonlinear Dynamic Analysis of Cable and Membrane Structure*. PhD thesis, Department of Civil Engineering, Oregon State University, 1982.

[7] NASA. Constellation: NASA's new spacecraft, Ares and Orion, 2008. http://www.nasa.gov/mission_pages/constellation/orion/index.html.

[8] NASA. NASA's mission statement, 2009. http://naccenter.arc.nasa.gov/NASAMission.html.

[9] C. Oravetz and T. Yechout. Experimental investigation of the wake characteristics of the NASA Orion capsule. In *46th AIAA Aerospace Sciences Meeting and Exhibit*, Reno, Nevada, 2008.

[10] E. Outen. NASA's airbag drop tests in full swing, 2008. http://www.nasa.gov/mission_pages/constellation/orion/2nd-gen-airbag-test.html.

[11] Y. Saad and M. Schultz. GMRES: A generalized minimal residual algorithm for solving nonsymmetric linear systems. *SIAM Journal of Scientific and Statistical Computing*, 7:856–869, 1986.

[12] SEED. Parachute: What is a cfm?, 2009. http://www.seed.slb.com/qa2/FAQView.cfm?ID=1197.

[13] K. Stein, R. Benney, V. Kalro, T. Tezduyar, J. Leonard, and M. Accorsi. Parachute fluid–structure interactions: 3-D Computation. *Computer Methods in Applied Mechanics and Engineering*, 190:373–386, 2000.

[14] K. Takizawa, J. Christopher, C. Moorman, S. Wright, J. Martin, and T. Tezduyar. Fluid–structure interaction modeling of the Orion spacecraft parachutes. In B. Schrefler, E. Onate, and M. Papadrakakis, editors, *Coupled Problems 2009*, Barcelona, Spain, 2009. CIMNE.

[15] T. Tezduyar. Stabilized finite element formulations for incompressible flow computations. *Advances in Applied Mechanics*, 28:1–44, 1992.

[16] T. Tezduyar. Computation of moving boundaries and interfaces and stabilization parameters. *International Journal for Numerical Methods in Fluids*, 43:555–575, 2003.

[17] T. Tezduyar. Finite element methods for fluid dynamics with moving boundaries and interfaces. In E. Stein, R. D. Borst, and T. Hughes, editors, *Encyclopedia of Computational Mechanics*, Volume 3: Fluids, chapter 17. John Wiley & Sons, 2004.

[18] T. Tezduyar. Finite elements in fluids: Stabilized formulations and moving boundaries and interfaces. *Computers & Fluids*, 36:191–206, 2007.

[19] T. Tezduyar, M. Behr, and J. Liou. A new strategy for finite element computations involving moving boundaries and interfaces – the deforming-spatial-domain/space–time procedure: I. The concept and the preliminary numerical tests. *Computer Methods in Applied Mechanics and Engineering*, 94(3):339–351, 1992.

[20] T. Tezduyar, M. Behr, S. Mittal, and J. Liou. A new strategy for finite element computations involving moving boundaries and interfaces – the deforming-spatial-domain/space–time procedure: II. Computation of free-surface flows, two-liquid flows, and flows with drifting cylinders. *Computer Methods in Applied Mechanics and Engineering*, 94(3):353–371, 1992.

[21] T. Tezduyar and Y. Osawa. Finite element stabilization parameters computed from element matrices and vectors. *Computer Methods in Applied Mechanics and Engineering*, 190:411–430, 2000.

[22] T. Tezduyar and S. Sathe. Modeling of fluid–structure interactions with the space–time finite elements: Solution techniques. *International Journal for Numerical Methods in Fluids*, 54:855–900, 2007.

[23] T. Tezduyar, S. Sathe, J. Pausewang, M. Schwaab, J. Christopher, and J. Crabtree. Fluid–structure interaction modeling of ringsail parachutes. *Computational Mechanics*, 43:133–142, 2008.

[24] T. Tezduyar, S. Sathe, J. Pausewang, M. Schwaab, J. Christopher, and J. Crabtree. Interface projection techniques for fluid–structure interaction modeling with moving-mesh methods. *Computational Mechanics*, 43:39–49, 2008.

[25] T. Tezduyar, S. Sathe, J. Pausewang, M. Schwaab, J. Crabtree, and J. Christopher. Air–fabric interaction modeling with the Stabilized Space–Time FSI technique. In *Proceedings of the Third Asian-Pacific Congress on Computational Mechanics (CD-ROM)*, Kyoto, Japan, 2007.

[26] T. Tezduyar, S. Sathe, K. Stein, and L. Aureli. Modeling of fluid–structure interactions with the space–time techniques. In H.-J. Bungartz and M. Schafer, editors, *Fluid–Structure Interaction*, volume 53 of *Lecture Notes in Computational Science and Engineering*, pages 50–81. Springer, 2006.

[27] T. Tezduyar, M. Schwaab, and S. Sathe. Sequentially-Coupled Arterial Fluid–Structure Interaction (SCAFSI) technique. *Computer Methods in Applied Mechanics and Engineering*, published online, DOI: 10.1016/j.cma.2008.05.024, July 2008.

[28] T. Tezduyar, K. Takizawa, and J. Christopher. Multiscale Sequentially-Coupled Arterial Fluid–Structure Interaction (SCAFSI) technique. In S. Hartmann, A. Meister, M. Schaefer, and S. Turek, editors, *International Workshop on Fluid–Structure Interaction — Theory, Numerics and Applications*. Kassel University Press, 2009.

[29] T. Tezduyar, K. Takizawa, J. Christopher, C. Moorman, and S. Wright. Interface projection techniques for complex FSI problems. In T. Kvamsdal, B. Pettersen,

P. Bergan, E. Onate, and J. Garcia, editors, *Marine 2009*, Barcelona, Spain, 2009. CIMNE.

[30] P. M. Wagner. Experimental measurement of parachute canopy stress during inflation, 1978. http://www.dtic.mil/cgi-bin/GetTRDoc?AD=ADA058474Location=U2doc=GetTRDoc.pdf.